Planet Formation in the Outer Solar System

Scott J. Kenyon

Smithsonian Astrophysical Observatory, 60 Garden Street, Cambridge, MA 02138

e-mail: skenyon@cfa.harvard.edu

ABSTRACT

This paper reviews coagulation models for planet formation in the Kuiper Belt, emphasizing links to recent observations of our and other solar systems. At heliocentric distances of 35–50 AU, single annulus and multiannulus planetesimal accretion calculations produce several 1000 km or larger planets and many 50–500 km objects on timescales of 10–30 Myr in a Minimum Mass Solar Nebula. Planets form more rapidly in more massive nebulae. All models yield two power law cumulative size distributions, $N_C \propto r^{-q}$ with $q = 3.0$–3.5 for radii $r \gtrsim 10$ km and $N_C \propto r^{-2.5}$ for radii $r \lesssim 1$ km. These size distributions are consistent with observations of Kuiper Belt objects acquired during the past decade. Once large objects form at 35–50 AU, gravitational stirring leads to a collisional cascade where 0.1–10 km objects are ground to dust. The collisional cascade removes 80% to 90% of the initial mass in the nebula in ~ 1 Gyr. This dust production rate is comparable to rates inferred for α Lyr, β Pic, and other extrasolar debris disk systems.

Subject headings: planetary systems – solar system: formation – stars: formation – circumstellar matter

1. INTRODUCTION

Recent observations indicate that nearly all low and intermediate mass stars are born with massive circumstellar disks of gas and dust. Most young pre-main sequence stars with ages of ~ 1 Myr have gaseous disks with sizes of 100 AU or larger and masses of $\sim 0.01\ M_\odot$ (Beckwith 1999; Lada 1999). Many older main sequence stars have dusty debris disks with sizes of 100–1000 AU (Aumann et al. 1984; Smith & Terrile 1984; Gaidos 1999; Habing et al. 1999; Song et al. 2000; Spangler et al. 2001). Current source statistics suggest the percentage of stars with observable disks declines from $\sim 100\%$ among the youngest stars to less than 10% for stars more than 1 Gyr old (Backman & Paresce 1993; Artymowicz 1997; Lada 1999; Lagrange et al. 2000).

Models for the formation of our solar system naturally begin with a disk. In the 1700's, Immanuel Kant and the Marquis de Laplace proposed that the solar system collapsed from a gaseous medium of roughly uniform density (Kant 1755; Laplace 1796). A flattened gaseous disk

– the protosolar nebula – formed out of this cloud. The Sun contracted out of material at the center of the disk; the planets condensed in the outer portions. Although other ideas have been studied since Laplace's time, this picture has gained widespread acceptance. Measurements of the composition of the earth, moon, and meteorites support a common origin for the sun and planets (e.g., Harris 1976; Anders & Grevesse 1989). Simulations of planet formation in a disk produce objects resembling known planets on timescales similar to the estimated lifetime of the protosolar nebula (Safronov 1969; Greenberg et al. 1978; Wetherill & Stewart 1993; Pollack et al. 1996; Alexander & Agnor 1998; Levison, Lissauer, & Duncan 1998; Kokubo & Ida 2000; Kortenkamp & Wetherill 2000; Chambers 2001).

The Kuiper Belt provides a stern test of planet formation models. In the past decade, observations have revealed several hundred objects with radii of 50–500 km in the ecliptic plane at distances of $\sim$ 35–50 AU from the Sun (Jewitt & Luu 1993; Luu & Jewitt 1996; Gladman & Kavelaars 1997; Jewitt et al. 1998; Chiang & Brown 1999; Luu et al. 2000; Gladman et al. 2001). The total mass in these KBOs, $\sim 0.1\ M_{\oplus}$, suggests a reservoir of material left over from the formation of our solar system (Edgeworth 1949; Kuiper 1951). However, this mass is insufficient to allow the formation of 500 km or larger KBOs on timescales of $\sim$ 5 Gyr (Fernández & Ip 1981; Stern 1995; Stern & Colwell 1997a; Kenyon & Luu 1998).

The Kuiper Belt also provides an interesting link between local studies of planet formation and observations of disks and planets surrounding other nearby stars. With an outer radius of at least 150 AU, the mass and size of the Kuiper Belt is comparable to the masses and sizes of many extrasolar debris disks (Backman & Paresce 1993; Artymowicz 1997; Lagrange et al. 2000). Studying planet formation processes in the Kuiper Belt thus can yield a better understanding of evolutionary processes in other debris disk systems.

Making progress on planet formation in the Kuiper Belt and the dusty disks surrounding other stars requires plausible theories which make robust and testable predictions. This paper reviews the coagulation theory for planet formation in the outer solar system (for reviews on other aspects of planet formation, see Mannings, Boss, & Russell 2000). After a short summary of current models for planet formation, I consider recent numerical calculations of planet formation in the Kuiper Belt and describe observational tests of these models. I conclude with a discussion of future prospects for the calculations along with suggestions for observational tests of different models of planet formation.

2. BACKGROUND

Figure 1 shows the geometry of the outer part of our solar system. Surrounding the Sun at the center, four colored ellipses indicate the orbits of Jupiter (red), Saturn (cyan), Uranus (green), and Neptune (dark blue). The black ellipse plots the orbit of Pluto, which makes two orbits around the Sun for every three of Neptune. Roughly 20% of currently known KBOs, the *plutinos*, have similar

orbits. The black dots represent 200 KBOs randomly placed in the *classical Kuiper Belt,* objects in roughly circular orbits outside the 3:2 resonance with Neptune. A few KBOs outside this band lie in the 2:1 orbital resonance with Neptune. The eccentric magenta ellipse indicates the orbit of one KBO in the *scattered Kuiper Belt* (Luu et al 1997). The total mass in classical KBOs is ~ 0.1 $M_\oplus$; the mass in scattered KBOs and KBOs in the 2:1 resonance may be comparable but is not so well constrained as the mass in classical KBOs (Trujillo et al. 2001a; Gladman et al. 2001).

Viewed edge-on, the orbits of the planets and the KBOs in our solar system lie in a disk with a height of $\sim$ 20–30 AU and a radius of $\sim$ 150–200 AU. Because a disk is the natural outcome of the collapse of a cloud with some angular momentum, this geometry formed the early basis of the nebular hypothesis. However, a cloud of gas and dust with the diameter of the Oort cloud, the mass of the Sun, and a modest rotation rate of $\Omega \sim 10^{-8}$ yr^{-1} has too much angular momentum to collapse to the Sun's present size. Building on previous realizations that a turbulent viscosity could move material inwards and angular momentum outwards through the protosolar nebula, von Weizsäcker (1943, 1948) developed the basic physics of a viscous accretion disk and solved this angular momentum problem (see also Lüst 1952; Shakura & Sunyaev 1973; Lynden-Bell & Pringle 1974).

Most planet formation theories now begin with a viscous accretion disk (Kenyon 1999; Mannings, Boss, & Russell 2000, and references therein). The natural evolutionary timescale is the viscous time scale, which measures the rate at which matter diffuses through the disk,

$$\tau_V \approx \frac{25,000 \text{ yr}}{\alpha} \left(\frac{A}{100 \text{ AU}} \right)^{5/4} . \tag{1}$$

This expression does not include a weak dependence on the mass of the central star. The viscosity parameter α measures the strength of the turbulence relative to the local thermal pressure. Most studies of disks in interacting binaries and other objects indicate $\alpha \sim 10^{-3}$ to 10^{-2}, which yields viscous timescales of 1–10 Myr at 100 AU (see Lin & Papaloizou 1995, 1996 for a review of the physics of accretion disks).

Another evolutionary timescale for the disk depends on an external source, the central star, instead of internal disk physics. Hollenbach et al. (1994) showed that high energy photons from a luminous central star can ionize the outer skin of the gaseous disk and raise the gas temperature to $\sim 10^4$ K (see also Shu, Johnstone, & Hollenbach 1993; Richling & Yorke 1997, 1998, 2000). The thermal velocity of this gas is large enough to overcome the local gravity beyond $\sim$ 10 AU for a 1 $M_\odot$ central star. Material then leaves the disk, producing a bipolar outflow which may be observed in nearby star-forming regions (Bally et al. 1998; Johnstone, Hollenbach, & Bally 1998). Disk evaporation occurs on a timescale

$$\tau_E \approx 10^7 \text{ yr} \left(\frac{M_d}{0.01 \text{ M}_\odot} \right) \left(\frac{A}{10 \text{ AU}} \right) \left(\frac{\phi_\star}{10^{41} \text{ s}^{-1}} \right)^{-1/2} , \tag{2}$$

where $\phi_\star$ is the flux of hydrogen-ionizing photons from the central star.

The evaporation time is sensitive to the spectral type of the central star. Early B-type stars with $\phi_\star \sim 10^{45}$ s^{-1} can evaporate disks in ~ 1 Myr or less. The Sun has an observed flux $\phi_\odot \sim 10^{38}$ s^{-1} (Vernazza, Avrett, & Loeser 1981), which leads to a long evaporation time, ~ 3 Gyr, for a disk with $A \sim 100$ AU. However, young solar-type stars are 2–3 orders of magnitude brighter than the Sun at ultraviolet and X-ray wavelengths (e.g., Dorren, Guedel, & Guinan 1995, and references therein). The disk evaporation time for a young solar-type star is therefore $\tau_E \approx 10$–100 Myr for $A \sim 10$–100 AU.

The evaporation and viscous timescales provide a rough upper limit to the lifetime of a gaseous disk surrounding a solar-type star. It is encouraging that both timescales are comparable to the disk lifetimes estimated from observations of gas and dust surrounding pre-main sequence stars in the solar neighborhood, $\tau_d \sim 1$–10 Myr (Russell et al. 1996; Hartmann et al. 1998; Lada 1999; Brandner et al. 2000; Haisch, Lada & Lada 2001). The observational timescales place strong constraints on planet formation models. Gas giants must form before the gas disappears. Rocky planets must form before the dust disappears. The observations constrain these timescales to 100 Myr or less.

Two theories – coagulation and dynamical instability – try to explain planet formation in a viscous disk. Coagulation theories propose that large dust grains decouple from the gas and settle to the midplane of the disk Safronov (1969); Lissauer (1993). These grains may then collide to form successively larger grains (Weidenschilling 1980; Weidenschilling & Cuzzi 1993) or continue to settle into a very thin layer which can become gravitationally unstable (Goldreich & Ward 1973). Both paths produce km-sized planetesimals which collide and merge to produce larger bodies (Weidenschilling 1984; Palmer, Lin, & Aarseth 1993). If the growth time is short compared to the viscous timescale in the disk, collisions and mergers eventually produce one or more 'cores' which accumulate much of the solid mass in an annular 'feeding zone' defined by balancing the gravity of the planetary core with the gravity of the Sun and the rest of the disk (e.g. Chambers 2001; Rafikov 2001, and references therein). Large cores with masses of 1–10 $M_\oplus$ accrete gas from the feeding zone (Pollack 1984; Pollack et al. 1996; Ikoma et al. 2001). In our solar system, this model accounts for the masses of the terrestrial and several gas giant planets (Lissauer 1987; Lissauer et al. 1996; Weidenschilling et al. 1997; Levison, Lissauer, & Duncan 1998; Bryden, Lin, & Ida 2000; Ida et al. 2000a; Inaba et al. 2001; Alexander, Boss, & Carlson 2001). Variants of this model, including orbital migration and other dynamical processes, can explain Jupiter-sized planets orbiting other solar-type stars (Weidenschilling & Marzari 1996; Lin & Ida 1997; Ward 1997; Ford, Rasio, & Sills 1999; Kley 2000). However, coagulation models barely succeed in making gas giant planets in 1–10 Myr, when observations suggest most of the gas may be gone.

Dynamical instability models develop the idea that part of an evolving disk can collapse directly into a Jupiter-mass planet (e.g., Ward 1989; Cameron 1995; Boss 1997, 2000). When the local gravity overcomes local shear and pressure forces, part of the disk begins to collapse. Cool material flows into the growing perturbation and aids the collapse. Eventually, the perturbation reaches planet-sized proportions by accumulating all of the gaseous and solid material in the feeding

zone. This model naturally forms large planets on timescales, $\sim 10^3$ to 10^5 yr, short compared to the evaporation or viscous timescales. However, dynamical instability models produce neither terrestrial planets in the inner disk nor icy bodies like Pluto in the outer disk. The disk mass required for a dynamical instability may also exceed the mass observed in pre-main sequence disks (Beckwith 1999; Lada 1999).

The 'Minimum Mass Solar Nebula' is an important starting point to test these and other planet formation models (Hoyle 1946; Weidenschilling 1977a; Hayashi 1981; Lissauer 1987; Bailey 1994). The Minimum Mass is based on the near equality between the measured elemental compositions of the earth, moon, and meteorites (Anders & Grevesse 1989, and references therein) and the relative abundances of heavy elements in the Sun (see the discussion in Harris 1976; Alexander, Boss, & Carlson 2001). This analysis leads to the hypothesis that the initial elemental abundances of the solar nebula were nearly identical to solar abundances. The surface density of the Minimum Mass Solar Nebula follows from adding hydrogen and helium to each planet to reach a solar abundance and spreading the resulting mass uniformly over an annulus centered on the present orbit of the planet.

Figure 2 shows how the surface mass density varies with distance for the Minimum Mass Solar Nebula. The arrows indicate the mass added to the terrestrial planets. The plot shows Venus, Earth, Jupiter, Saturn, Uranus, Neptune, and the Kuiper Belt. When the material at the orbits of Venus and Earth is augmented to reach a solar abundance of hydrogen, the surface density for the gas follows the solid curve, $\Sigma_g \approx \Sigma_0 (A/1 \text{ AU})^{-3/2}$, out to $A \approx 10$ AU and then decreases sharply. The solid curve in Figure 2 has $\Sigma_0 = 1500$ g cm^{-2}; for comparison, Hayashi, Nakazawa, & Nakagawa (1985) concluded $\Sigma_0 = 1700$ g cm^{-2} while Weidenschilling (1977a) proposed $\Sigma_0 = 3200$ g cm^{-2}. Following Hayashi (1981), the dot-dashed curve representing the mass density of solid material has

$$\Sigma_s = \begin{cases} 7 \text{ g cm}^{-2} \ (A/1 \text{ AU})^{-3/2} & A \leq 2.7 \text{ AU} \\ \\ 30 \text{ g cm}^{-2} \ (A/1 \text{ AU})^{-3/2} & A > 2.7 \text{ AU} \end{cases} \tag{3}$$

The uncertainties in the coefficients are a factor of ~ 2. The change in the surface density of solid material at 2.7 AU corresponds to the region where ice condenses out of the gas in the Hayashi (1981) model. The location of this region depends on the disk structure (Sasselov & Lecar 2000).

The Minimum Mass Solar Nebula was one of the great successes of early viscous accretion disk theories, because steady-state disk models often yield $\Sigma \propto A^{-3/2}$. The sharp decrease in the "observed" Σ at 10–30 AU supports photoevaporation models where ionized hydrogen becomes unbound at ~ 10 AU (Shu, Johnstone, & Hollenbach 1993). Current abundance measurements for the gas giants lend additional evidence: the gas-to-dust ratio appears to decrease with heliocentric distance in parallel with the surface density drop beyond 10 AU (Pollack 1984; Podolak, Young,

& Reynolds 1985; Podolak & Reynolds 1987; Pollack et al. 1996). In the Kuiper Belt, there may be two origins for the large drop in the observed surface density from a $\Sigma \propto A^{-3/2}$ model. Adding H and He to achieve a solar abundance at 30–40 AU increases the mass in the Kuiper Belt by a factor of ~ 30. Material lost to orbital dynamics and to high velocity collisions of objects in the Belt may increase the current mass by another factor of 10–100 (e.g. Holman & Wisdom 1993; Davis & Farinella 1997), bringing the initial surface density in the Kuiper Belt within range of the $\Sigma \propto A^{-3/2}$ line. If these estimates are correct, the total mass of the Minimum Mass Solar Nebula is ~ 0.01 $M_\odot$ for an outer radius of ~ 100 AU, close to the median mass for circumstellar disks surrounding young stars in nearby regions of star formation (Lada 1999).

Figure 2 suggests that the Kuiper Belt provides an important test of coagulation models. Forming objects with radii of ~ 500–1000 km requires ~ 10–100 Myr at ~ 40 AU in a Minimum Mass Solar Nebula (see below). The outermost gas giant, Neptune, must form on a similar timescale to accrete gas from the solar nebula before the gas escapes (equations (1–2)). Neptune formation places another constraint on the KBO growth time; Neptune inhibits KBO formation at 30–40 AU by increasing particle random velocities on timescales of 20–100 Myr (Holman & Wisdom 1993; Levison & Duncan 1993; Duncan et al. 1995; Malhotra 1996; Morbidelli & Valsecchi 1997). Kenyon & Luu (1998, 1999a,b) investigated how KBOs form by coagulation and compared their results with observations (see also Fernández 1997; Stern & Colwell 1997a, 1997b). The next section briefly describes the model results; §4 compares these results with observations.

3. Kuiper Belt Models

3.1. Coagulation Calculations

Safronov (1969) invented the current approach to planetesimal accretion calculations. In his particle-in-a-box method, planetesimals are a statistical ensemble of masses with a distribution of horizontal and vertical velocities about a Keplerian orbit (see also Greenberg et al. 1978; Ohtsuki, Nakagawa, & Nakazawa 1988; Wetherill & Stewart 1989; Spaute et al. 1991; Stern 1995; Kenyon & Luu 1998). Because n-body codes cannot follow the 10^{15} or more small planetesimals required in a typical coagulation calculation, the statistical approximation is essential. The model provides a kinetic description of the collision rate in terms of the number density and the gravitational cross-section of each type of planetesimal in the grid. Treating planetesimal velocities as perturbations about a Keplerian orbit allows the use of the Fokker-Planck equation to solve for changes in the velocities due to gravitational interactions and physical collisions.

In our implementation of Safronov's model, we begin with a differential mass distribution, $n(m_i)$, in concentric annuli centered at heliocentric distances, A_j, from a star of mass $M_\star$ (Kenyon & Luu 1999a; Kenyon & Bromley 2001, 2002). The mass distribution has N mass batches in each annulus; $\delta_i \equiv m_{i+1}/m_i$ is the mass spacing between batches. To provide good estimates of the growth time, our calculations have $\delta = 1.1$–2.0 (Ohtsuki & Nakagawa 1988; Wetherill 1990;

Kolvoord & Greenberg 1992; Kenyon & Luu 1998). To evolve the mass and velocity distributions in time, we solve the coagulation and energy conservation equations for an ensemble of objects with masses ranging from $\sim 10^7$ g to $\sim 10^{26}$ g. We adopt analytic cross-sections to derive collision rates, use the center-of-mass collision energy to infer the collision outcome (merger, merger + debris, rebound, or disruption), and compute velocity changes from gas drag (Adachi et al. 1976; Weidenschilling 1977b; Wetherill & Stewart 1993), Poynting-Robertson drag (Burns, Lamy, & Soter 1979; Kary, Lissauer, & Greenzweig 1993), and collective interactions such as dynamical friction and viscous stirring using a Fokker-Planck integrator (Stewart & Kaula 1980; Hornung, Pellat, & Barge 1985; Barge & Pellat 1990; Wetherill & Stewart 1993; Luciani, Namouni, & Pellat 1995; Ohtsuki 1999; Stewart & Ida 2000). The code reproduces previous calculations for accretion at 1 AU (Wetherill & Stewart 1993; Weidenschilling et al. 1997), collisional disruption of pre-existing large KBOs at 40 AU (Davis & Farinella 1997), and n-body simulations of gravitational scattering at 1 AU (see Kenyon & Bromley 2001, and references therein).

During the early stages of planet formation, particle-in-a-box algorithms yield good solutions to the coagulation equation (Ida & Makino 1992; Kokubo & Ida 1996; Lee 2000; Malyshkin & Goodman 2001). Most published calculations have been made for a single accumulation zone to get a good understanding of the basic physics without spending a large amount of computer time (e.g., Greenberg et al. 1978; Ohtsuki, Nakagawa, & Nakazawa 1988; Wetherill & Stewart 1989; Stern 1996a; Kenyon & Luu 1998). Single annulus calculations provide the basis for estimates of planetary growth rates as a function of heliocentric distance and initial disk mass (Lissauer 1987; Wetherill & Stewart 1993; Lissauer et al. 1996). Multiannulus calculations allow bodies in neighboring accumulation zones to interact and thus provide better estimates of planetary growth rates (Spaute et al. 1991; Kenyon & Bromley 2002). These codes enable calculations with additional physics, such as orbital migration, which cannot be incorporated accurately into single annulus codes. Once large objects form, one-on-one collisions become important; statistical estimates for collision cross-sections and gravitational stirring in single and multiannulus codes begin to fail. More detailed n-body calculations are then required to study the evolution of the largest objects.

In the following sections, I discuss published single annulus models for Kuiper Belt objects and then outline new multiannulus calculations.

3.2. Single Annulus Models

Our Kuiper Belt models begin with an input cumulative size distribution

$$N_C \propto r_i^{-q_i}, \tag{4}$$

with initial radii $r_i = 1$–80 m and $q_i = 3$. These particles are uniformly distributed in a single annulus with a width of 6 AU at 32–38 AU from the Sun. The total mass in the annulus is M_0; $M_0 \approx 10\ M_\oplus$ for a Minimum Mass Solar Nebula. All mass batches start with the same initial eccentricity e_0 and inclination $i_0 = e_0/2$. The adopted mass density, $\rho_0 = 1.5$ g cm^{-3}, is appropriate for icy

bodies with a small rocky component (Greenberg 1998). These bodies have an intrinsic tensile strength S_0 which is independent of particle size and a total strength equal to the sum of S_0 and the gravitational binding energy (Davis et al. 1985, 1994). Kenyon & Luu (1999a, 1999b) describe these parameters in more detail.

Figure 3 shows the results of a complete coagulation calculation for $M_0 = 10\ M_\oplus$, $e_0 = 10^{-3}$, and $S_0 = 2 \times 10^6$ erg g^{-1} (see also Stern 1996a; Stern & Colwell 1997a, 1997b). We separate the growth of KBOs into three regimes. Early in the evolution, frequent collisions damp the velocity dispersions of small bodies. Rapid growth of these bodies erases many of the initial conditions, including q_i and e_0 (Kenyon & Luu 1998, 1999). These bodies slowly grow into 1 km objects on a timescale of 5–10 Myr $(M_0/10\ M_\oplus)^{-1}$. The timescale is sensitive to the initial range of sizes; because collisional damping is important, models starting with larger objects take longer to reach runaway growth. The linear growth phase ends when the gravitational range of the largest objects exceeds their geometric cross-section. Gravitational focusing enhances the collision rate by factors of $(V_e/V_c)^2 \approx 10$–1000, where V_c is the collision velocity and V_e is the escape velocity of a merged object. The largest objects then begin "runaway growth" (e.g., Greenberg et al. 1978; Wetherill & Stewart 1993), where their radii grow from ~ 1 km to $\gtrsim 100$ km in several Myr. During this phase, dynamical friction and viscous stirring increase the velocity dispersions of the smallest bodies from ~ 1 m s^{-1} up to ~ 40 m s^{-1}. This velocity evolution reduces gravitational focusing factors and ends runaway growth. The largest objects then grow slowly to 1000+ km sizes on timescales that again depend on the initial mass in the annulus. Kokubo & Ida (1998) call this last phase in the evolution 'oligarchic growth' to distinguish it from the linear and runaway growth phases (see also Ida & Makino 1993).

The shapes of the curves in Figure 3 show features common to all coagulation calculations (e.g., Wetherill & Stewart 1989; Stern & Colwell 1997a,b; Weidenschilling et al. 1997, Davis, Farinella, & Weidenschilling 1999). Almost all codes produce two power-law size distributions. The merger component at large sizes has $q_f \approx 3$; the debris component at small sizes has $q_f = 2.5$ (Dohnanyi 1969; Tanaka et al. 1996). Dynamical friction produces a power law velocity distribution in the merger component. The debris component has roughly constant velocity, because it contains a small fraction of the initial mass. The transition region between the two components usually has a 'bump' in the size distribution, where objects which can merge grow rapidly to join the merger population (Davis & Farinella 1997; Davis et al. 1999). Calculations for annuli closer to the Sun also yield a 'runaway' population, a plateau in the size distribution of the largest objects (Wetherill & Stewart 1993). The objects in this plateau contain most of the mass remaining in the annulus (Wetherill & Stewart 1993; Weidenschilling et al. 1997). In our models, the largest 10–20 objects are not massive enough to produce a 'runaway plateau' in the size distribution until the very late stages of the evolution (see below).

Our Kuiper Belt calculations yield one result which is very different from coagulation calculations for annuli at less than 10 AU from the Sun. In all other published calculations, the largest bodies contain most of the initial mass in the annulus. In the Kuiper Belt, most of the initial mass

ends up in 1 km objects. Fragmentation and gravitational stirring are responsible for this difference between calculations at 1–10 AU and at 40 AU. In our calculations, fragmentation produces a large reservoir of small bodies that damp the velocity dispersions of the large objects through dynamical friction. These processes allow a short runaway growth phase where 1 km objects grow into 100 km objects. Continued fragmentation and velocity evolution damp runaway growth by increasing the velocity dispersions of small objects and reducing gravitational focusing factors. Our models thus enter the phase of 'oligarchic growth' earlier than models for planet growth at 1–10 AU. This evolution leaves $\sim$ 1%–2% of the initial mass in 100–1000 km objects. The remaining mass is in 0.1–10 km radius objects. Continued fragmentation gradually erodes these smaller objects into dust grains that are removed from the Kuiper Belt on short timescales, $\sim 10^7$ yr (Backman & Paresce 1993; Backman, Dasgupta, & Stencel 1995; Davis & Farinella 1997; Davis et al. 1999). Thus, in our interpretation, 100–1000 km radius objects comprise a small fraction of the original Kuiper Belt.

Planet formation in the outer parts of a solar system is self-limiting. During the late stages of planetesimal evolution, large planets stir smaller objects up to the shattering velocity. This process leads to a collisional cascade, where planetesimals are ground down into smaller and smaller objects. Continued fragmentation, radiation pressure, and Poynting-Robertson drag then remove small particles from the disk faster than large objects can accrete. Because the shattering velocity depends on the tensile strength of a planetesimal, collisional cascades start sooner when planetesimals are weaker. The maximum mass of an icy object in the outer solar system thus depends on its strength (Figure 4). At 35–140 AU, our calculations yield a linear relation between the maximum radius and the intrinsic strength of a planetesimal,

$$\log r_{max} \approx 2.45 - 0.09 \log(a_i/35 \text{ AU}) + 0.22 \log S_0 , \tag{5}$$

for planetesimals with $\log S_0 = 1$–6 (Kenyon & Luu 1999a).

The weak variation of r_{max} with heliocentric distance is a new result based on calculations for this review. If planetesimals all have the same strength, the shattering velocity is independent of heliocentric distance. Once small planetesimals reach the shattering velocity, the largest objects do not grow. Because planetesimals at larger heliocentric distances are less bound to the central star, a massive planet at large a_i stirs small planetesimals more effectively than the same planet in orbit at small a_i. Small planetesimals in the outer part of the disk thus require relatively less stirring to reach the shattering velocity than small planetesimals in the inner part of the disk. A less massive planet in the outer disk can stir planetesimals to the shattering limit as effectively as a more massive planet in the inner disk. Hence, larger objects form in the inner disk than in the outer disk.

The initial mass M_0 is the main input parameter which establishes the formation timescale and the mass distribution of KBOs in the outer solar system. Figure 5 illustrates the time variation of the model parameter r_5, defined as the radius where the cumulative number of objects exceeds 10^5 (Kenyon & Luu 1999a). Most surveys estimate $\sim 10^5$ KBOs with radii of 50 km or larger; the

r_5 parameter thus provides a convenient way to compare theory with observations. Figure 5 shows that r_5 increases steadily with time during the linear growth phase. The number of 50 km radius KBOs increases dramatically during runaway growth and then approaches a roughly constant value during oligarchic growth. More massive models enter runaway growth sooner; the timescale for r_5 to reach 50 km is

$$\tau(r_5 = 50 \text{ km}) \approx 10 \text{ Myr } (M_0/10 \ M_\oplus)^{-1} \tag{6}$$

More massive disks also produce more 50 km radius KBOs. Based on Figure 5, protosolar nebulae with less than 30% of the Minimum Mass produce too few 50 km radius KBOs; nebulae with more than ~ 3 times the Minimum Mass may produce too many.

The timescale for Pluto formation at 35 AU is also sensitive to the initial population of bodies with radii of 1 km or smaller. Collisional damping of these small bodies leads to an early runaway growth phase where 0.1–1 km bodies grow rapidly to sizes of 100 km or larger. Because collisional damping is ineffective for bodies with radii 1–10 km or larger, calculations which exclude small bodies take at least a factor of 3 longer to reach runaway growth (Kenyon & Luu 1998). These models also fail to achieve a shallow power-law size distribution with $q_f = 3$ until late in the oligarchic growth phase (e.g., Davis et al. 1999).

Pluto formation is remarkably insensitive to other initial conditions in the disk. Growth by mergers, collisional damping, and dynamical friction rapidly erase the initial size and velocity distributions. As long as particle strengths exceed a minimum value of 300 erg g^{-1}, the details of the fragmentation algorithm do not affect planetesimal growth significantly. Formation times change by a factor of two or less for order of magnitude changes in the fragmentation parameters and the initial size and velocity distributions (Kenyon & Luu 1999a, 1999b).

3.3. Multiannulus calculations

Multiannulus calculations address some of the limitations and uncertainties of coagulation models in a single accumulation zone (Spaute et al. 1991; Weidenschilling et al. 1997). By including long-range interactions between objects in neighboring annuli, a multiannulus code yields better treatment of velocity evolution and more accurate estimates for the accretion rates of large bodies. The improvement resulting from a multiannulus code scales with the number of annuli. More annuli allow a more accurate treatment of collision cross-sections and velocity evolution (Kenyon & Bromley 2001, 2002).

To illustrate some results from our multiannulus code, I describe two calculations of large planetesimals in the Kuiper Belt. The calculations begin with 0.1–1.0 km objects in 16 annuli at distances of 40–54 AU from the Sun. The planetesimals have an initial eccentricity $e_0 = 2 \times 10^{-3}$ and a tensile strength $S_0 = 2 \times 10^6$ erg g^{-1}. The debris receives a small fraction, $f_{KE} = 0.05$, of the impact kinetic energy. The calculations do not include gas drag or Poynting-Robertson drag. During the 1–5 Gyr of each calculation, drag forces have negligible impact on the evolution of

objects with radii of 0.1 km or larger.

Figure 6 illustrates the time evolution of the size and horizontal velocity distributions for a model with fragmentation (Greenberg et al. 1984; Davis et al. 1985; Kenyon & Luu 1999a) and velocity evolution (Stewart & Ida 2000; Kenyon & Bromley 2001). During the first 20 Myr of this calculation, collisions damp the velocity dispersions of the smallest bodies. Planetesimals grow slowly from 1 km to ~ 10 km. When objects are larger than ~ 10 km, gravitational focusing enhances collision rates. The largest objects then grow rapidly to sizes of ~ 200–300 km. Dynamical friction and viscous stirring heat up the orbits of the smallest objects. This evolution reduces gravitational focusing factors and ends runaway growth. A handful of large objects then grow slowly; their sizes reach ~ 1000 km at 70 Myr and ~ 3000 km at ~ 120 Myr.

The lower panel of Figure 7 illustrates the evolution of the largest body in each annulus. Collisions are most rapid in the inner annuli; objects at 40 AU thus grow faster than objects at 50 AU. Runaway growth begins first at 40 AU (10–20 Myr), when objects at 55 AU have grown by less than a factor of two. After 30 Myr, the largest objects at 40 AU have radii of ~ 100 km and then grow slowly to radii of ~ 1000 km during the oligarchic growth phase. This evolution is delayed at 50 AU. During runaway growth, objects at 50–55 AU grow from sizes of ~ 10 km at 30–50 Myr to ~ 100–200 km at 50–70 Myr. After ~ 100 Myr, the largest objects in all annuli grow slowly at roughly the same pace.

Objects grow much more slowly in models without fragmentation and velocity evolution (Figure 7, top panel). During the first 300 Myr of the calculation, planetesimals grow slowly from ~ 1 km to ~ 10 km. Because particle velocities are constant, gravitational focusing factors change little. Once particle sizes reach ~ 100 km, runaway growth begins in the innermost two annuli. A few large bodies rapidly accrete most of the mass in each annulus. At ~ 500 Myr, the largest body in the second annulus accretes the largest body in the first annulus and then consumes the rest of the bodies in annuli 1–5. Large bodies in annuli 6–8 begin runaway growth at ~ 700 Myr. A single large body in annulus 7 consumes all of the bodies in annuli 6–10. This process repeats for annuli 11–13 at ~ 1 Gyr, when a single large body in annulus 11 grows almost as large as the bodies in annuli 2 and 7. The remaining objects in annuli 14–16 probably form a fourth large object at $\sim$ 1.3 Gyr; we terminated the calculation before this point.

Figure 8 compares the evolution of the largest bodies in each calculation. Collisional damping dominates the velocity evolution of small particles at 40–55 AU (see also Kenyon & Luu 1998, 1999a). Dynamical friction provides additional damping to the largest bodies. Smaller particle velocities produce larger gravitational focusing factors and more rapid growth rates. Models with velocity evolution thus enter the runaway growth phase earlier (~ 10–30 Myr) than models without velocity evolution (~ 300–500 Myr). During runaway growth, viscous stirring dominates the velocity evolution of all particles. Larger particle velocities yield smaller gravitational focusing factors and smaller growth rates. By removing small particles from the grid, fragmentation reduces growth rates further. Thus, the largest bodies reach a maximum size which depends on the strength of

the smallest bodies and the heliocentric distance (Figure 4; see also Kenyon & Luu 1999a). In models without velocity evolution, gravitational focusing factors grow with the mass of the largest body. Thus, models without velocity evolution produce a few very massive objects. The orbital separation of these massive objects is roughly their gravitational range. In our calculations, this limit is ~ 2.4 Hill radii; $R_H = (m_p/3\ M_\odot)^{1/3}$, where m_p is the mass of the planet.

The results for KBO formation in these initial multiannulus calculations are encouraging. Successful KBO models need to form $\sim 10^5$ KBOs and at least one Pluto before Neptune attains its present mass at ~ 25 AU (e.g., Kenyon & Luu 1998, 1999a). If the gas in the solar nebula is depleted on timescales of 5–10 Myr, Neptune must form on similar timescales (Bryden, Lin, & Ida 2000). Some recent numerical calculations of gas accretion onto rocky cores can achieve this goal (Fernández & Ip 1984; Ip 1989; Pollack et al. 1996; Bryden, Lin, & Ida 2000). Although our Pluto formation timescale of 60–70 Myr is long compared to these constraints, single annulus calculations starting from smaller bodies, 1–100 m in size, form Pluto and numerous KBOs on timescales of 10–20 Myr (Figures 3 and 5; Kenyon & Luu 1999a). Scaling the single annulus models suggests formation timescales of 5–20 Myr at 40–50 AU with a multiannulus code.

3.4.   Long term evolution

Several processes shape the long-term evolution of KBOs in the outer solar system (Holman & Wisdom 1993; Backman, Dasgupta, & Stencel 1995; Davis & Farinella 1997; Teplitz et al. 1999; Davis et al. 1999; Kuchner, Brown, & Holman 2002). Once Neptune attains its current mass and location, gravitational perturbations pump up orbital velocities and begin to remove KBOs of all sizes from the Kuiper Belt. Gravitational stirring by the largest KBOs increases orbital velocities of smaller KBOs to the shattering limit. Once a collisional cascade begins, the largest objects do not grow significantly. Small objects are shattered and then removed from the Kuiper Belt by radiation pressure and Poynting-Robertson drag.

To begin to understand how these processes have shaped the current population of KBOs, several groups have calculated the long-term collisional evolution of large objects in the Kuiper Belt. Davis & Farinella (1997) used a single annulus code to show that the observed population of KBOs with radii of 25–50 km or larger can survive disruptive collisions for 5 Gyr at 40–50 AU (Stern 1996b; Stern & Colwell 1997a, 1997b). These objects are thus remnants of the original population formed during the early evolution of the Kuiper Belt. For reasonable values of S_0, smaller KBOs are collision fragments produced during the collisional cascade. Davis et al. (1999) confirmed these results. For $t > 1$ Gyr, the Davis et al. (1999) calculations yield a very steep power law size distribution for the merger population, $q_f \approx 11$. This result differs from the results of single annulus codes and the multiannulus result in Figure 6. The source of this difference is uncertain but may be due to different treatments of velocity evolution or fragmentation.

Figures 9–10 illustrate how the size distribution evolves at late times in our multiannulus

calculations. The first model is a continuation of the calculation for Fig. 6; the second model repeats this calculation for weak bodies with $S_0 = 10^3$ erg g^{-1}. The first 70–100 Myr of this second calculation closely follows the evolution of the first model. Runaway growth at 40–50 AU produces 10 km bodies in 20 Myr and 100 km bodies in 30 Myr. Slower oligarchic growth leads to 1000 km bodies at 70 Myr (40 AU) to 100 Myr (50 AU). At 70 Myr, the amount of debris produced from collisional erosion of the small bodies is negligible, $\sim 6\%$ of the mass at the start of the calculation.

Models with strong, icy particles (Fig. 9; $S_0 = 2 \times 10^6$ erg g^{-1}) have a long oligarchic growth phase followed by a collisional cascade. The largest objects grow from $r_i \sim 1000$ km at $t = 70$ Myr to $r_i \sim 3000$ km at $t = 300$ Myr to $r_i \sim 6000$ km at $t = 1$ Gyr. This slow growth phase produces a power-law size distribution, with $q_f \approx 3.35$ for $r_i = 20$–6000 km. As the largest bodies reach sizes of 2000–6000 km, viscous stirring slowly increases the eccentricities of the smallest objects from $e \approx 0.01$ at 70 Myr to $e \approx 0.05$ at 300 Myr to $e \approx 0.09$ at $t = 1$ Gyr. Throughout most of this phase, collisions between small objects produce debris through cratering; this debris is $\sim 10\%$ of the initial mass at 300 Myr and $\sim 70\%$ of the initial mass at 1 Gyr. Cratering removes the bump in the size distribution for $r_i \sim 1$ km. Just before 1 Gyr, collisional disruption begins to deplete the population of 0.1–1 km bodies on timescales of ~ 100 Myr. This evolution starts to produce a dip in the size distribution at $r_i \approx 1$ km.

Collisional cascades begin sooner in models with weak bodies (Fig. 10; $S_0 = 10^3$ erg g^{-1}). Cratering is not important in these models; most mass is lost through collisional disruption of small bodies. During the first 70 Myr of evolution, cratering is responsible for less than 1% of the mass loss; collisional disruption removes $\sim 6\%$ of the initial mass. After 70 Myr, objects grow slowly as more and more material is lost to collisional disruption. The largest object has a radius of ~ 2000 km at 300 Myr and ~ 3000 km at 1 Gyr. The size distribution for the largest bodies follows a power law with $q_f \approx 3.15$ for $r_i = 20$ km to 2000–3000 km. For smaller bodies, collisional disruption produces a pronounced dip in the size distribution at 0.3–1.0 km. The debris lost to bodies with $r_i < 0.1$ km (the smallest object in the grid) is $\sim 65\%$ of the initial mass at 300 Myr and $\sim 85\%$ of the initial mass at 1 Gyr.

These multiannulus calculations confirm some of the single annulus results. The size of the largest object at 40–50 AU depends on the tensile strength of 0.1–10 km objects. Stronger small bodies allow the growth of larger large bodies (Figure 4; Kenyon & Luu 1999a). We plan additional calculations to see whether the size-strength relation is similar to equation (5); preliminary results suggest a shallower relation. Gravitational stirring by 1000 km and larger objects in the grid leads to a collisional cascade, where cratering and collisional disruption remove small bodies from the grid (see also Davis & Farinella 1997; Davis et al. 1999; Stern & Colwell 1997a, 1997b). The duration of the collisional cascade is ~ 100 Myr to ~ 1 Gyr (see also Kenyon & Bromley 2001). Collisions convert $\sim 80\%$ to 90% of the initial mass in the grid to small particles with sizes of 100 m or smaller. Disruptive collisions and Poynting-Robertson drag can remove this material from the Kuiper Belt on short timescales, ~ 10–100 Myr (Backman et al. 1995; Stern 1996b; Teplitz et al. 1999).

During the late stages of our multiannulus calculations, the size distribution for the largest objects follows a power law with $q_f = 3.15$–3.35. Once the largest objects have radii of ~ 1000 km or larger, the slope of the power law size distribution is nearly invariant. We plan additional calculations to test the sensitivity of the slope to initial conditions and the fragmentation parameters.

4. OBSERVATIONAL TESTS OF COAGULATION MODELS

Observations provide powerful constraints on the KBO population. Sensitive imagers on large ground-based and space-based telescopes detect individual large objects directly. Current instrumentation yields direct detections of 50 km objects from the ground and 10 km objects from the *Hubble Space Telescope (HST)*. Future large ground-based 30-m to 100-m telescopes and the *Next Generation Space Telescope (NGST)* will improve these limits by an order of magnitude or more. The population of smaller KBOs with radii of ~ 1 km can be estimated indirectly from the frequency of short-period comets and from dynamical calculations. The population of KBOs with sizes smaller than ~ 0.1 km can only be derived as an ensemble by measuring the surface brightness of the sky and eliminating other radiation sources. Despite confusion from the galaxy and the local Zodiac, optical and far-infrared (far-IR) observations provide useful measures of the population of dust grains in the Kuiper Belt.

These data allow broad observational tests of KBO formation models. The large sample of individual KBO detections provides a good measurement of KBO number counts, the number of KBOs per magnitude per square degree projected on the sky. For an adopted albedo ω_l for large KBOs, the number counts directly yield the KBO size distribution for objects with radii of 50 km or larger (Jewitt et al. 1998; Luu & Jewitt 1998; Chiang & Brown 1999; Gladman et al. 2001). The radial distribution of large KBOs follows from the size distribution and heliocentric distances derived from the orbit or from an adopted albedo (Dones 1997; Allen et al. 2001; Trujillo & Brown 2001; Trujillo et al. 2001a). Surface brightness measurements constrain the size distribution of small KBOs. Far-IR data measure thermal emission from small grains in the Kuiper Belt; optical and near-IR data measure scattered light. Deriving constraints on the size distribution from surface brightness data requires an assumption about the grain albedo ω_g, which may differ from ω_l.

4.1. Number Counts

The observed number counts of bright KBOs follow a simple relation

$$\log N = \alpha(R - R_0) \ , \tag{7}$$

where N is the cumulative number of bodies brighter than magnitude R (Gladman et al. 1998; Jewitt et al. 1998; Chiang & Brown 1999). Recent fits to the observations suggest $\alpha = 0.65$–0.70 and $R_0 = 23.3$–23.5 (Gladman et al. 2001; Trujillo et al. 2001b). If the size distribution of KBOs

is independent of heliocentric distance and if all KBOs have the same albedo, a power-law relation for the number counts implies a power-law size distribution,

$$\log N_C = N_0 \left(\frac{r}{r_0}\right)^{-q} ,$$ (8)

where N_C is the cumulative number of objects with radius larger than r and $q = 5\alpha$ (Jewitt et al. 1998; Chiang & Brown 1999; Gladman et al. 2001). Fits to the observations thus imply size distributions with $q = 3.25$–3.50. The characteristic radius r_0 is related to R_0; the scaling factor N_0 depends on the total mass in the Kuiper Belt.

Kenyon & Luu (1999b) show that complete coagulation calculations produce power law size distributions for large KBOs. For a wide range of input parameters, single annulus models yield $q = 2.75$–3.25 for KBOs with radii of $\sim$ 10–1000 km (see Table 2 of Kenyon & Luu 1999b). To construct predicted number counts, Kenyon & Luu (1999b) adopt $\omega_l = 0.04$ and the slope parameter, $g = 0.15$, in the standard two parameter magnitude relation for asteroids (Bowell et al 1989). An adopted heliocentric distance d and a random phase angle β from the Sun then specify the observed R magnitude for a KBO with radius r_i. The slope parameter g relates the brightness of an asteroid at solar phase angle β to the brightness at opposition, $\beta = 0°$. Kenyon & Luu (1999b) assume that the KBO size distribution is independent of heliocentric distance, with 50% of the KBOs in a ring at 42–50 AU and the rest as Plutinos at 39.4 ± 0.2 AU. The resulting number counts are insensitive to the Plutino fraction and the outer radius of the ring.

The upper panel of Figure 11 compares predicted with observed number counts from several single annulus calculations. Data are as indicated in the legend. Error bars for the measured points are typically a factor of 2–3 and are not shown for clarity. The lines plot predicted number counts for models with $e_0 = 10^{-3}$ and $M_0 \approx 0.3$ (dot-dashed), 1.0 (solid), and 3.0 (dashed) times the Minimum Mass Solar Nebula. Models with different e_0 are indistinguishable for $R \leq 27$ (Kenyon & Luu 1999b). The model luminosity functions agree well with current observations.

Multiannulus calculations also produce power-law size distributions for large KBOs (Figures 6 and 9–10). For several completed calculations, these models yield steeper slopes, $q = 3.2$–3.5, for the size distribution of objects with radii of 10–1000 km. These results are much closer to the observed slopes than the multiannulus calculations of Davis et al. (1999). We plan additional multiannulus calculations to measure the scatter in the predicted slope of the size distribution. To construct an initial model for the number counts, I use radial distributions of KBOs derived from the coagulation code and adopt $e = 0$ and $\beta = 0$ for all sources. This model assumes all sources are found at opposition and neglects bright KBOs closer than 40 AU.

The lower panel of Figure 11 compares observed number counts with predictions for several multiannulus calculations. The data are the same in both panels. The lines show predicted number counts for multiannulus models with an initial mass in solid material equal to the Minimum Mass Solar Nebula. The solid curve indicates counts when the first Plutos form at 40–45 AU. The other curves plot counts at 1 Gyr for models where the tensile strength of small objects is $S_0 = 10^3$ erg

g^{-1} (dot-dashed curve) and $S_0 = 2 \times 10^6$ erg g^{-1} (dashed curve). For $R \geq 20$, model counts at 1 Gyr are independent of S_0. Models with stronger planetesimals produce larger planets and thus predict more objects with $R \leq 20$ at 1 Gyr.

The good agreement between models and observations for R = 20–26 in Figure 11 is encouraging. When the first Plutos form at 40–45 AU in the multi-annulus calculations, the predicted number counts follow a linear relation between log N and R (equation (7)) with $\alpha = 0.80 \pm 0.01$ and $R_0 = 22.45 \pm 0.05$. After 1 Gyr, the slope of the number counts is $\alpha = 0.65 \pm 0.02$, much closer to the value derived from the data, $\alpha = 0.65$–0.70 (Gladman et al. 2001). The normalization derived for the models, $R_0 = 21.95 \pm 0.10$, is roughly a magnitude larger than the measured $R_0 = 23.0$–23.5. However, these models do not include loss of KBOs by dynamical interactions with Neptune. At 40–50 AU, these dynamical losses range from $\sim 50\%$ to $\sim 80\%$ of the initial mass in the Kuiper Belt (e.g., Holman & Wisdom 1993; Levison & Stern 1995). Applying these losses to our 1 Gyr number count models yields $R_0 \sim 22.70$–23.70, passably close to the observed value.

4.2. KBOs and Olbers Paradox

Many KBOs are too faint to be detected as individual objects even with large telescopes. All together, these faint KBOs can produce a detectable diffuse background light. Optical and near-IR data measure the amount of scattered light from faint KBOs; far-IR and submm data measure the amount of thermal emission. The KBO background light is smaller than diffuse emission from the local Zodiac (Leinert et al. 1998) and has not been detected (Backman et al. 1995; Stern 1996b; Teplitz et al. 1999). Nevertheless, the upper limits on scattered and thermal emission provide interesting constraints on the population of small KBOs.

Measured optical and far-IR sky surface brightnesses demonstrate that KBO number counts cannot follow equation (7) to arbitrarily faint magnitudes. For equation (7) with $\alpha > 0.4$, the optical sky surface brightness of KBOs brighter than magnitude R is (Kenyon & Windhorst 2001):

$$\mu_R = 41.03 - 2.5 \log\left(\frac{\alpha}{\alpha - 0.4}\right) + (1 - 2.5\alpha)\,(R - R_0)\,. \tag{9}$$

This surface brightness exceeds the measured sky surface brightness in the ecliptic plane,[1] $\mu_R \approx 22$ mag arcsec^{-2}, at $R \approx 45$–55 for $\alpha \approx 0.6$–0.75 (Windhorst, Mathis, & Keel 1992; Windhorst et al. 1994; Windhorst, Keel, & Pascarelle 1998; Biretta et al. 2000; Kenyon & Windhorst 2001). For an adopted albedo ω_g and temperature T_{KBO}, the thermal background from small KBOs depends

---

[1]The observed flux of the Zodiacal light decreases away from the ecliptic plane as csc β where β is the ecliptic latitude. Using the measured surface brightness at $\beta = 30°$, the approximate vertical thickness of the KBO distribution, does not change the main conclusions of this section.

only on the optical surface brightness

$$I_\nu(\text{FIR}) \lesssim 9.5 \times 10^{17-0.4\mu_R} \ T_{KBO}^{-1} \ \left(\frac{1-\omega_g}{\omega_g} \right) \ \text{Jy sr}^{-1} \ . \tag{10}$$

This result assumes that a small KBO emits less radiation than the maximum flux of a blackbody with temperature T_{KBO}. For $\omega_g \approx 0.5$, small KBOs with $\mu_R \gtrsim 22$ mag arcsec^{-2} and $T_{KBO} \approx 40$ K (Backman, Dasgupta, & Stencel 1995; Teplitz et al. 1999) have $I_\nu \lesssim 4 \times 10^7$ Jy sr^{-1}. This limits exceeds the measured far-IR background of $I_\nu(\text{FIR}) \lesssim 1$–$2 \times 10^6$ Jy sr^{-1} for wavelengths longer than $\sim 10 \ \mu$m (Fixsen et al. 1998; Hauser et al. 1998). The known, finite sky brightnesses at optical and far-IR wavelengths thus imply a turnover in the KBO number counts for $R \gtrsim 30$ (Kenyon & Windhorst 2001).

Previous support for a turnover in the KBO number counts has relied on theoretical interpretations of available observations (see Weissman & Levison 1997). From numerical simulations, Levison & Stern (1995) show that KBOs can excite an eccentricity in the Pluto-Charon orbit. If perturbations from KBOs are the dominant source of the eccentricity, the measured e yields an upper limit to the number of KBOs with radii of 20–300 km. Orbital integrations of known Jupiter-family comets suggest an origin in the Kuiper Belt (Duncan et al. 1988; Levison & Duncan 1994; Duncan et al. 1995; Duncan & Levison 1997; Ip & Fernández 1997). If the Kuiper Belt is the source of all Jupiter-family comets, the number of known Jupiter-family comets and lifetimes derived from the orbital integrations provide limits on the number of KBOs with radii of 1–10 km. These limits indicate that there are a factor of ten fewer KBOs with radii of 1–100 km than suggested by a simple extrapolation of equation (7) to $R \gtrsim 27$.

The coagulation calculations provide more theoretical support for a turnover in the number counts. Models with fragmentation predict two power-law size distributions, a merger population with $q = 3$ at large radii and a debris population with $q = 2.5$ at small radii (Figures 6 and 9–10; Stern & Colwell 1997a; Davis et al. 1999; Kenyon & Luu 1999a). The transition radius depends on the tensile strength of small objects. For $S_0 \sim 10^3$ to 10^7 erg g^{-1}, this radius is $\sim$ 1–100 km (Davis & Farinella 1997; Davis et al. 1999; Kenyon & Luu 1999a), which agrees with the turnover radius derived from dynamical constraints.

To place another constraint on the turnover radius, Kenyon & Windhorst (2001) construct a physical model for the surface brightness of small KBOs. They adopt a broken-power law size distribution,

$$N_C(r) = \begin{array}{ll} n_0(r/r_0)^{-q_1} & r > r_0 \\ \\ n_0(r/r_0)^{-q_2} & r \le r_0 \end{array} \tag{11}$$

and assume objects lie in a ring around the Sun with surface density $\Sigma \propto A^{-\gamma}$. The ring has an inner radius $A_1 = 40$ AU and an outer radius $A_2 = 50$ AU. The optical counts set n_0 and q_1. For an adopted ω_g, μ_R results from a sum over all objects projected into a box with an area of 1 arcsec^2. For thermal emission, Kenyon & Windhorst (2001) adopt the Backman & Paresce (1993) relations

to derive grain temperatures as a function of A and sum the thermal emission from all objects in a solid angle of 1 steradian.

Kenyon & Windhorst (2001) demonstrate a clear turnover in the KBO number counts (Figure 12). Small KBOs with radii of 1 μm to $\sim$ 1 km must have a size distribution with $q \sim 3.4$ or less to satisfy the known limits on the sky-surface brightness at optical and far-infrared wavelengths.

Figure 12 shows how the optical and 100 μm surface brightness increase with fainter KBO R-band magnitude. Solid lines show results when all objects have $\omega_g = 0.04$; dot-dashed lines show how the surface brightness changes when the albedo varies smoothly from $\omega_g = 0.04$ for $r \geq 1$ km to $\omega_g = 0.5$ for $r \leq 0.1$ km. Larger albedos produce brighter optical surface brightnesses and a fainter far-IR surface brightness. For models with $q_2 = 3.5$, KBOs with a small constant albedo have a limiting $\mu_R \sim 24.5$ mag arcsec^{-2}, fainter than the observed sky brightness. If small KBOs have $a_2 = 3.5$ and a large albedo, the predicted μ_R exceeds the observed background at $R \sim 70$ mag. This limit corresponds to objects with $r \sim 0.03$ mm. In both cases, the far-IR surface brightness exceeds the measured sky brightness for $\lambda \leq 240$ μm at $R \approx 65$–70 mag. The predicted far-IR surface brightness lies below measured limits at longer wavelengths.

A direct detection of diffuse light from KBOs would begin to provide more stringent tests of coagulation models. Measurements of the variation of the diffuse light with ecliptic latitude or longitude would yield the scale height and orbital distribution of small KBOs. The sensitivity of archival deep HST WFPC2 images can improve constraints on the KBO optical background by a factor of ten. The *Space Infrared Telescope Facility* may improve the far-IR constraints by a similar factor. The *Next Generation Space Telescope* will provide direct detections of individual KBOs near the proposed knee in the size distribution at $R \approx 28$–31 mag and more accurate background measurements in the optical and near-IR. These and other facilities will yield better tests of model predictions for the size distribution of small KBOs.

4.3.   Radial distribution of KBOs

The radial distribution of KBOs provides direct constraints on several physical processes in the outer solar system. KBOs in the 2:1, 3:2, and other orbital resonances yield information on dynamical interactions between small bodies and gas giant planets (Holman & Wisdom 1993; Duncan et al. 1995; Hahn & Malhotra 1999, Kuchner et al 2002). KBOs in the scattered Kuiper Belt allow tests of models for the formation of the Oort comet cloud. KBOs in the classical Kuiper Belt constrain the initial surface density and the formation history of large objects. Here, I concentrate on the radial distribution of classical KBOs, where coagulation models can offer some insight into the observations.

The observed radial distribution of KBOs in the classical Kuiper Belt is uncertain. Secular resonances with Neptune and Uranus truncate the inner edge of the classical Kuiper Belt at $\sim$ 41 AU (Duncan et al. 1995). Because the first surveys detected no KBOs outside 50 AU, Dones

(1997) proposed an outer edge to the classical Kuiper Belt at ~ 50 AU. Several large-angle surveys for KBOs provide support for an abrupt outer edge at 48–50 AU (Jewitt et al. 1998; Allen et al. 2001; Trujillo et al. 2001a). Trujillo & Brown (2001) analyze discovery data for the apparent magnitude and heliocentric distance of all KBOs and derive an outer edge at 47 ± 1 AU. They conclude that plausible variations of the slope of the size distribution, the maximum radius, and the albedo cannot produce the observed edge. Gladman et al. (2001) note that recent, unpublished surveys identify distant KBOs more frequently than older surveys, and conclude that the radial distribution of KBOs may continue smoothly beyond 48 AU.

Coagulation theory provides some explanations for possible origins of an outer edge to the observed radial distribution of classical KBOs. Because the formation timescale for large objects depends on the orbital period, the size of the largest object is a sensitive function of heliocentric distance, a. For $t < 100$ Myr, multiannulus calculations yield $r_{max} \propto a^{-3}$ (Figure 7). This result implies a factor of two variation in the size of the largest object from $a = 40$ AU to $a = 50$ AU. After 100 Myr, the difference can be (a) enhanced, if gravitational stirring by large objects at the inner edge of the Kuiper Belt prevents the growth of objects farther out in the Belt, or (b) diminished if gravitational stirring by Neptune and other giant planets preferentially slows growth of large objects at the inner edge of the Belt.

The size distribution is an important factor in understanding the reliability of an edge in the observed radial distribution of KBOs. Monte Carlo simulations of the observations demonstrate that the edge is more robust for shallower input size distributions (Jewitt et al. 1998; Allen et al. 2001; Trujillo & Brown 2001; Gladman et al. 2001). For the $q = 3$ power law size distribution derived from single annulus coagulation models, the edge is much more obvious than for the $q = 3.25$ power law derived from multiannulus calculations. Several test calculations suggest that q grows with a. If this conclusion holds with additional calculations, the coagulation models favor steeper size distributions at larger distances in the Kuiper Belt. If this variation is real, the evidence for an outer edge to the Kuiper Belt is more questionable.

Unless the tensile strength of objects decreases with a, the variation of r_{max} with S_0 from equation (5) is insufficient to yield a large variation in the radial distribution of KBOs. If S_0 is independent of a, r_{max} changes by less than 30% at 40–50 AU. Trujillo & Brown (2001) show that this small change cannot produce the observed lack of KBOs beyond 48 AU. A factor of 10 change of S_0 at 40–50 AU can produce factor of 2–3 changes in r_{max}. Because the magnitude of S_0 for KBOs is not well-known, quantifying changes of S_0 with other variables in the model is pointless. Deriving tensile strengths of different comet families might help to quantify possible variations of S_0 with a (see below).

To make an initial theoretical prediction for the radial distribution of classical KBOs based on the coagulation models, I use the number counts for multiannulus models from Figure 11 at 1 Gyr. The model assumes circular orbits, but does not include collisional or dynamical evolution from 1 Gyr to the present. If this evolution is independent of a, then the model provides a reasonable

first approximation to the present situation in the outer solar system. For simplicity, I quote the result of this model as a ratio, N(40–47 AU)/N(47–54 AU). For a limiting magnitude $R = 27$, the multiannulus model with $S_0 = 2 \times 10^6$ erg g^{-1} has N(40–47 AU)/N(47–54 AU) = 3; the model with $S_0 = 10^3$ erg g^{-1} has N(40–47 AU)/N(47–54 AU) = 2. Due to small number statistics, models with brighter limiting magnitudes produce unreliable results. Because deeper surveys sample more of the size distribution, the number ratio declines as the limiting magnitude increases.

The results of the coagulation models suggest some caution in the interpretation of the apparent edge in the radial distribution of KBOs beyond 47 AU. Factor of 2–3 declines in the apparent number of KBOs with a are a natural outcome of coagulation models when the input surface density follows a Minimum Mass Solar Nebula. Larger changes are possible, if the surface density declines more rapidly or with plausible changes to KBO properties as a function of a. Larger surveys to $R = 28$ or deeper surveys to $R = 29$–30 should yield better statistics to discriminate among the possibilities.

A robust comparison between the models and observations is difficult due to uncertain observational biases and to uncertain long-term dynamical evolution of the initial KBO population. Most KBO surveys concentrate on regions near the ecliptic plane, where the success rate is larger; distant KBOs may have a different inclination distribution from nearby KBOs Brown (2001). The model estimates are smaller than the observed fraction, N(40–47 AU)/N(47–54 AU) $\approx$ 4–6 (Trujillo & Brown 2001; Gladman et al. 2001). The model assumes no migration in a and no changes in i from 1 Gyr to 5 Gyr; dynamical models show that interactions with Neptune and other gas giant planets change a, e, and i on short timescales.

4.4. Orbital elements of KBOs

The distributions of e and i yield information on the long-term dynamical evolution of KBOs. Numerical integrations of KBO orbits indicate that dynamical interactions with the gas giant planets dramatically change the orbital elements of objects in the outer solar system (e.g., Torbett & Smoluchowski 1990; Holman & Wisdom 1993; Duncan et al. 1995; Malhotra 1996; Levison & Duncan 1997; Morbidelli & Valsecchi 1997, Kuchner et al. 2002). This gravitational sculpting of the KBO population produces several dynamical KBO populations, including classical KBOs, plutinos and other resonant KBOs, and scattered KBOs (e.g., Malhotra 1995; Gladman et al. 2001). Understanding how these phenomena produce the current e and i distributions of KBOs remains a major puzzle.

Coagulation calculations provide an important foundation for understanding the distributions of KBO orbital elements. Because the giant planets are also condensing out of the solar nebula, dynamical interactions between KBOs and gas giants are unimportant during the early stages of KBO growth. Collisional damping and dynamical friction thus set the early velocity evolution of the KBO population. These processes produce nearly circular orbits for large objects, $e \lesssim 0.001$ for $r_i \approx 100$–1000 km, and modestly eccentric orbits for smaller objects, $e \sim 0.01$ for $r_i \lesssim 10$

km (Figures 9–10). Once the collisional cascade begins, viscous stirring dominates the velocity evolution. The orbits of all objects become more eccentric and more highly inclined. After ~ 1 Gyr, large objects in the multiannulus calculations have $e \sim 0.02$ for $S_0 = 10^3$ erg g^{-1} models and $e \sim 0.1$ for $S_0 = 2 \times 10^6$ erg g^{-1} models. Both models have $i/e \approx 0.4$. These results indicate that KBOs probably have significant e and i without dynamical interactions with gas giant planets.

This conclusion is probably insensitive to initial conditions in the Kuiper Belt. Kenyon & Bromley (2001) show that 100–500 km objects can stir up velocities significantly on timescales of 1–5 Gyr in a Minimum Mass Solar Nebula. Thus, large KBOs with sizes of 500–1000 km can stir up other KBOs to large e and i on a 1 Gyr timescale. If KBOs form in a low mass solar nebula, stirring timescales are longer, ~ 5 Gyr for 1000 km objects with 10% of the Minimum Mass and ~ 50 Gyr for 1000 km objects with 1% of the Minimum Mass. Thus, our scenario for producing KBOs in a Minimum Mass Solar Nebula leads to KBOs with large e and i. Models which form massive KBOs in a low mass solar nebula yield KBOs with low e and i.

These results indicate that gravitational sculpting and the internal dynamics of KBOs are important in creating the current distributions of a, e, i for KBOs[2]. Viscous stirring between large KBOs broadens the e and i distributions with time; gravitational sculpting by the gas giants broadens the e and i distributions *and* selects stable ranges of e and i. Careful treatment of both processes is necessary to understand the current orbital elements of KBO populations.

5. DISCUSSION AND SUMMARY

The discovery of the Kuiper Belt in the 1990's provides fundamental constraints on models for the formation and evolution of planets in the outer parts of our solar system. The observations imply $\sim 10^5$ KBOs with radii of 50–500 km and a total mass of ~ 0.1–0.2 $M_\oplus$ beyond the orbit of Neptune. The theoretical challenge is to understand the formation of large objects in a current reservoir of material that is $\sim 1\%$ of the initial mass in the solar nebula. This goal assumes that KBOs formed locally and that the initial surface density of the solar nebula did not decease abruptly beyond the orbit of Neptune. Observations indicate typical disk radii of at least 100–200 AU in nearby pre-main sequence stars, which suggests that the disk of our solar system originally continued smoothly beyond the orbit of Neptune. Testing the assumption of local KBO formation relies on future comparisons between observations and theory.

Coagulation calculations appear to meet the challenge posed by KBOs. Published numerical calculations demonstrate that the formation of a few Plutos and numerous 100–500 km KBOs in the outer parts of a solar system is inevitable (Stern 1995, 1996a; Stern & Colwell 1997a; Davis et al. 1999; Kenyon & Luu 1999a). For a variety of initial conditions, collisions between small bodies at 30–50 AU naturally produce larger objects. Once there is a range in sizes, dynamical

---

[2]Gravitational interactions with passing stars can also modify the orbital elements of KBOs (Ida et al. 2000b).

friction efficiently reduces the orbital eccentricities of the largest objects. Large objects in nearly circular orbits grow quickly. At 30–50 AU, runaway growth can produce 100 km and larger objects on short timescales. These objects then grow slowly to radii of 1000 km or more.

The initial disk mass sets the timescale for Pluto formation in the outer parts of a solar system. Objects grow faster in more massive disks. For single annulus calculations of planetesimals orbiting the Sun, the timescale to produce the first Pluto is

$$t_P \approx 20 \text{ Myr } \left(\frac{\Sigma_{35}}{0.2 \text{ g cm}^{-2}} \right)^{-1} \, , \tag{12}$$

where $\Sigma_{35} \approx 0.2$ g cm^{-2} is the initial surface density of a minimum mass solar nebula model extrapolated into the Kuiper Belt at ~ 35 AU (Figure 2; see also Stern & Colwell 1997a; Kenyon & Luu 1999a). This timescale depends weakly on the initial conditions. Growth is more rapid in a solar nebula with small initial eccentricities and with small initial bodies (Kenyon & Luu 1999a).

The growth timescale in the Kuiper Belt is smaller than expected from coagulation calculations in the inner solar system. Lissauer et al. (1996) estimate a timescale to produce Moon-sized (10^{26} g) objects as

$$t_M \approx 0.5 \text{ Myr } \left(\frac{1 \text{ g cm}^{-2}}{\Sigma(a)} \right) \left(\frac{a}{1 \text{ AU}} \right)^{3/2} \, . \tag{13}$$

This relation implies timescales of ~ 500 Myr at 35 AU and ~ 1 Gyr at 45 AU. Our single annulus models yield $t_M \sim 100$ Myr at 35 AU and $t_M \sim 600$ Myr at 70 AU. For calculations where the initial size distribution is composed of 1–10 km bodies, multiannulus models imply $t_M \sim 200$–300 Myr at 40–50 AU. Collisional damping causes the difference between our results and equation (13). In our calculations, collisional damping between small objects with radii of 1 m to 1 km reduces eccentricities by factors of 5–10. Dynamical friction couples the eccentricity reduction of the small bodies to the largest bodies. Because runaway growth begins when gravitational focusing factors are large, collisional damping in our Kuiper Belt models leads to an early onset of runaway growth relative to models of the inner solar system where the collisional evolution of small bodies is not important.

Once large objects form in the outer part of a solar system, they stir up the velocities of small objects with radii of 10–100 km or less. Velocity stirring retards growth and produces debris. When the collision energy of small bodies is comparable to their tensile strength, the small bodies undergo a collisional cascade where planetesimals are ground down into smaller and smaller objects. This process produces numerous small grains which are ejected by radiation pressure ($\lesssim$ 1–3 μm grains) or pulled towards the Sun by Poynting-Robertson drag ($\gtrsim$ 1–3 μm grains). These grains are lost on short timescales of 1 Myr or less. When the collisional cascade begins, most of the mass in the outer solar system is contained in small objects that are easy to fragment. The collisional cascade thus robs the larger bodies of material. Because collisional cascades start sooner in the evolution when bodies are weaker, the size of the largest object in a calculation depends on the tensile strength of

the small planetesimals. Our models yield Earth-sized objects in the Kuiper Belt for $S_0 = 2 \times 10^6$ erg g^{-1} and Pluto-sized objects for $S_0 = 10^2$ to 10^3 erg g^{-1}.

The theoretical models thus resolve the dilemma of large objects in a low mass Kuiper Belt. Runaway growth of small objects at 40–50 AU in the solar nebula places $\sim$ 5%–10% of the initial mass in large objects with radii of 50–500 km or larger. The collisional cascade converts 80%–90% of the initial mass into debris which is removed from the Kuiper Belt on short timescales. Over the 4.5 Gyr lifetime of the solar system, gravitational interactions between KBOs and the gas giant planets can remove $\sim$ 50% to 80% of the remaining mass. Given the uncertainties, collisions and dynamics appear capable of removing more than 90% of the original mass in the Kuiper Belt.

The observed size distribution of KBOs provides strong observational tests of this picture. The final size distribution of a Kuiper Belt calculation has three components. The merger component at large sizes is a power-law with $q_f \approx$ 3.0–3.5; the debris component at small sizes is a power law with $q_f \lesssim 2.5$. The collisional cascade depletes objects with intermediate sizes of 0.1–10 km. Depletion produces a dip in the size distribution for $S_0 \lesssim 10^5$ erg g^{-1}.

The observations of large KBOs generally agree with the power law slope predicted for the merger component. The data are consistent with $q =$ 3.3–3.5; the multiannulus models predict q = 3.15–3.35. If dynamical interactions and collisional evolution continue to remove KBOs from the 40–50 AU annulus after 1 Gyr, the predicted number of KBOs is within a factor of two of the observed number of KBOs. The multiannulus calculations produce more KBOs with radii of 1000 km or larger than are observed with current surveys. The predicted number of these large objects depends on S_0 and is therefore uncertain. The observed number of large objects is plagued by small number statistics. Future surveys will provide robust constraints on the population of large objects. Improved multiannulus coagulation calculations which include dynamical interactions with gas giant planets will improve the predictions.

Current constraints on the population of small KBOs are also consistent with model predictions. The data indicate a turnover in the KBO number counts, which implies a turnover in the size distribution for small objects. The derived turnover radius of 0.1–10 km is close to theoretical predictions. Better observations of the optical and far-IR surface brightnesses of the Kuiper Belt can provide better estimates of the slope of the size distribution for KBOs with radii of 1 mm to 1 m. Observations with larger telescopes may detect the turnover radius directly.

Measuring the tensile strengths of comets provides an interesting test of this picture of KBO formation. In our models, the formation of Pluto by coagulation requires a tensile strength $S_0 \gtrsim$ 400 erg g^{-1}. Large tensile strengths, $S_0 \gtrsim 10^5$ erg g^{-1}, allow the formation of large bodies, $\sim$ 2000–3000 km, which have not been detected in the outer solar system. Because objects with radii of 2000–3000 km can form before Neptune reaches its current mass, the lack of large KBOs implies $S_0 \lesssim 10^4$ erg g^{-1} in the coagulation theory. Estimates on the tensile strength derived from comet Shoemaker-Levy 9, $S_0 \sim 10^2$ erg g^{-1} to 10^4 erg g^{-1} (e.g. Greenberg, Mizutani, & Yamamoto 1995), are close to the lower limit required to form Pluto. Theoretical estimates have a much larger

range, $S_0 \sim 10^2$ erg g^{-1} to 10^6 erg g^{-1} (Sirono & Greenberg 2000). As theoretical estimates improve and observations of disrupted comets become more numerous, these results can constrain the coagulation models.

The coagulation calculations demonstrate that planet formation in the outer parts of other solar systems is also inevitable. The mass of a Minimum Mass Solar Nebula is comparable to the median disk mass derived for nearby pre-main sequence stars (Beckwith 1999; Lada 1999; Mannings, Boss, & Russell 2000). The formation timescale for a 1000 km planet at 30–50 AU in one of these disks is therefore $\sim$ 10–30 Myr. Although this planet cannot be observed directly, gravitational stirring leads to a collisional cascade and copious dust production. In the multiannulus models, dust is produced at a rate of roughly 0.1–1 Earth mass every 100 Myr (see also Kenyon & Bromley 2002).

Observations of nearby debris disk systems are consistent with dust produced in a planet-forming disk. The sizes of debris disks, $\sim$ 10–1000 AU, are similar to the radius of the Kuiper Belt. The ages of the youngest debris disk systems are comparable to the Pluto formation timescale of $\sim$ 10–20 Myr (Lagrange et al. 2000). If the timescale for Poynting-Robertson drag sets the residence time for 1 μm and larger dust grains in the disk, the instantaneous dust mass in the disk is $\sim$ 0.1–1 lunar masses. This mass is comparable to the dust masses inferred from IR observations of debris disk systems such as α Lyr and β Pic (Backman & Paresce 1993; Lagrange et al. 2000). Finally, the duration of the collisional cascade in our Kuiper Belt models, $\sim$ 100 Myr to $\sim$ 1 Gyr, is similar to the estimated lifetimes of debris disk systems, $\sim$ 500 Myr (Habing et al. 1999, 2001). Kenyon & Bromley (2001) derive a similar predicted lifetime for debris disk systems from the coagulation equation (see also Kenyon 2000).

To make the connection between KBOs and debris disks more clear, Kenyon et al. (1999) investigate planet formation in the dusty ring of HR 4796A (Jayawardhana et al. 1998; Koerner et al. 1998; Augereau et al. 1999; Schneider et al. 1999; Greaves et al. 2000). They show that a planetesimal disk with a mass of 10–20 times the mass of the Minimum Mass Solar Nebula can form a dusty ring on 10–20 Myr timescales, comparable to the estimated age of HR 4796A. The model ring has a radial optical depth $\sim$ 1, in agreement with limits derived from infrared images and from the excess infrared luminosity. Although the initial mass in this single annulus calculation is large, multiannulus calculations suggest similar timescales with much smaller masses.

Finally, multiannulus calculations are an important new tool in developing a robust model for planet formation. Current computer technology allows practical multiannulus calculations that cover roughly a decade in disk radius. We are thus 1–2 orders of magnitude from constructing model grids of complete solar systems. Faster computers should resolve this difficulty in the next few years and allow us to consider the interfaces between (i) gas giants and terrestrial planets and (ii) gas giants and the Kuiper Belt. With some limitations, current multiannulus calculations promise predictions for the radial variation of the disk scale height (Kenyon & Bromley 2001) and the disk luminosity (Kenyon & Bromley 2002) as a function of stellar age, disk mass, and other

physical parameters. Detailed comparisons between these predictions and observations of debris disks will yield interesting constraints on the physics of planet formation in other solar systems. Applying these results to our solar system will provide a better idea how the Earth and other planets in our solar system came to be.

REFERENCES

Adachi, I., Hayashi, C., & Nakazawa, K. 1976, Progress of Theoretical Physics 56, 1756

Alexander, C. M. O'D., Boss, A. P., & Carlson, R. W. 2001, Sci, 293, 64

Alexander, S. G., & Agnor, C. B. 1998, Icarus, 132, 113

Allen, R. L., Bernstein, G. M., & Malhotra, R. 2001, ApJ, 549, L241

Anders, E., & Grevesse, N. 1989, Geochimica et Cosmochimica Acta, 53, 197

Artymowicz, P. 1997, ARE&PS, 25, 175

Augereau, J. C., Lagrange, A.-M., Mouillet, D., Papaloizou, J. C. B., & Grorod, P. A. 1999, A&A,
    348, 557

Aumann, H. H. et al., 1984, ApJ, 278, L23

Backman, D. E., Dasgupta, A., & Stencel, R. E. 1995, ApJ, 450, L35

Backman, D. E., & Paresce, F. 1993, in Protostars and Planets III, ed. E. H. Levy & J. I. Lunine
    (Tucson: Univ of Arizona), p. 1253

Bailey, M. 1994, in Asteroids, Comets, Meteors 1993, ed. A. Milani, M. DiMartino, & A. Cellino
    (Dordrecht: Kluwer), p. 443

Bally, J., Sutherland, R. S., Devine, D., & Johnstone, D. 1998, AJ, 116, 293

Barge, P., & Pellat, R. 1990, Icarus, 85, 481

Beckwith, S. V. W. 1999, in The Physics of Star Formation and Early Stellar Evolution, ed. by C.
    J. Lada & N. Kylafis (Dordrecht, Kluwer), p. 579

Biretta, J. A., et al. 2000, WFPC2 Instrument Handbook, Version 5.0 (Baltimore: STScI)

Boss, A. P. 1997, Science, 276, 1836

Boss, A. P. 2000, ApJ, 536, 101

Bowell, E., Hapke, B., Domingue, D., Lumme, K., Peltoniemi, J., & Harris, A. W. 1989, in Asteroids
    II, ed. by R. P. Binzel, T. Gehrels, & M. S. Matthews (Tucson: Univ. of Arizona), p. 524.

Brandner, W., et al. 2000, AJ, 120, 950

Brown, M. E. 2001, AJ, 121, 2804

Bryden, G., Lin, D. N. C., & Ida, S. 2000, ApJ, 544, 481

Burns, J. A., Lamy, P. L., & Soter, S. 1979, Icarus, 40, 1

Cameron, A. G. W. 1995, Meteoritics, 30, 133

Chambers, J. E. 2001, Icarus, 152, 205

Chiang, E. I., & Brown, M. E. 1999, AJ, 118, 1411

Cochran, A. L., Levison, H. F., Tamblyn, P., Stern, S. A., & Duncan, M. 1998, ApJ, 455, L89

Davis, D. R., Chapman, C. R., Weidenschilling, S. J., & Greenberg, R. 1985, Icarus, 62, 30

Davis, D. R., & Farinella, P. 1997, Icarus, 125, 50

Davis, D. R., Farinella, P., & Weidenschilling, S. J. 1999, in Lunar and Planetary Science XXX (Houston: Lunar Planetary Inst.), No. 1883

Dohnanyi, J. W. 1969, J. Geophys. Res., 74, 2531

Dones, L. 1997, in ASP Conf. Ser 122, From Stardust to Planetesimals, ed. Y. J. Pendleton & A. G. G. M. Tielens (San Francisco: ASP), p. 347

Dorren, J. D., Guedel, M. & Guinan, E. F. 1995, ApJ, 448, 431

Duncan, M. J., & Levison, H. F. 1997, Science, 276, 1670

Duncan, M. J., Levison, H. F., & Budd, S. M. 1995, AJ, 110, 3073

Duncan, M., Quinn, T., & Tremaine, S. 1988, ApJL, 328, L69

Edgeworth, K. E. 1949, MNRAS, 109, 600

Farinella, P., Paolicchi, P., & Zappalá, V. 1992, A&A, 253, 604

Fernández, J. A. 1997, Icarus, 129, 106

Fernández, J. A., & Ip, W.-H. 1981, Icarus, 47, 470

Fernández, J. A., & Ip, W.-H. 1984, Icarus, 58, 109

Fixsen, D. J., Dwek, E., Mather, J. C., Bennett, C. L. & Shafer, R. A. 1998, ApJ, 508, 123

Ford, E. B., Rasio, F. A., & Sills, A. 1999, ApJ, 514, 411

Gaidos, E. J. 1999, ApJ, 510, L131

Gladman, B., & Kavelaars, J. J. 1997, A&A, 317, L35

Gladman, B., Kavelaars, J. J., Nicholson, P. D., Loredo, T. J., & Burns, J. A. 1998, AJ, 116, 2042

Gladman, B., Kavelaars, J. J., Petit, J.-M., Morbidelli, A., Holman, M., & Loredo, T. J. 2001, AJ, 122, 1051

Goldreich, P., & Ward, W. R. 1973, ApJ, 183, 1051

Greaves J. S., Mannings V. & Holland, W. S. 2000, Icarus, 143, 155

Greenberg, J. M. 1998, A&A, 330, 375

Greenberg, J. M., Mizutani, H., & Yamamoto, T. 1995, A&A, 295, L35

Greenberg, R., Wacker, J. F., Hartmann, W. K., & Chapman, C. R. 1978, Icarus, 35, 1

Greenberg, R., Weidenschilling, S. J., Chapman, C. R., & Davis, D. R. 1984, Icarus, 59, 87

Habing, H. J., et al. 1999, Nature, 401, 456

Habing, H. J., et al. 2001, A&A, 365, 545

Hahn, J. M., & Malhotra, R. 1999, AJ, 117, 3041

Haisch., K. E., u Lada, E. A., & Lada, C. J. 2001, ApJ, 553, L153

Harris, A. W. 1976, in The Origin of the Solar System, ed. S. F. Dermott (New York: Wiley), p. 469

Hartmann, L., Calvet, N., Gullbring, E., & D'Alessio, P. 1998, ApJ, 495, 385

Hauser, M. G. et al. 1998, ApJ, 508, 25

Hayashi, C. 1981, Prog Theor Phys Suppl, 70, 35

Hayashi, C., Nakazawa, K., & Nakagawa, Y. 1985, in Protostars and Planets II, ed. D. C. Black & M. S. Mathews (Tucson: Univ. Arizona), p. 1100

Hollenbach, D. J., Johnstone, D., Lizano, S., & Shu, F. 1994, ApJ, 428, 654

Holman, M. J., & Wisdom, J. 1993, AJ, 105, 1987

Hornung, P., Pellat, R., & Barge, P. 1985, Icarus, 64, 295

Hoyle, F. 1946, MNRAS, 106, 406

Ida, S., Bryden, G., Lin, D. N. C., & Tanaka, H. 2000a, ApJ, 534, 428

Ida, S., Larwood, J., & Burkert, A. 2000, ApJ, 528, 351

Ida, S., & Makino, J. 1992, Icarus, 96, 107

Ida, S., & Makino, J. 1993, Icarus, 106, 210

Ikoma, H., Emori, H., & Nakazawa, K. 2001, ApJ, 553, 999

Inaba, S. H., Tanaka, H., Nakazawa, K., Wetherill, G. W., & Kokubo, E. 2001, Icarus, 149, 235

Ip, W.-H. 1989, Icarus, 80, 167

Ip, W.-H., & Fernández, J. A. 1997, A&A, 324, 778

Irwin, M., Tremains, S., & dotZytkow, A. N. 1995, AJ., 110, 3082

Jayawardhana, R. et al. 1998, ApJ, 503, L79

Jewitt, D., & Luu, J. 1993, Nature, 362, 730

Jewitt, D., Luu, J. X., & Trujillo, C. 1998, AJ, 115, 2125

Johnstone, D., Hollenbach, D., & Bally, J. 1998 ApJ, 499, 758

Kant, I. 1755, Universal Natural History and Theories of the Heavens

Kary, D. M., Lissauer, J. J., & Greenzweig, Y. 1993, Icarus, 106, 288

Kenyon, S. J. 1999, in The Physics of Star Formation and Early Stellar Evolution, ed. C. J. Lada & N. Kylafis (Dordrecht: Kluwer), p. 613

Kenyon, S. J. 2000, in ASP Conf. Ser. 231, Tetons 4: Galactic Structure, Stars, and the Interstellar Medium, ed. C. E. Woodward, M. D. Bicay, & J. M. Shull (San Francisco: ASP), p. 594

Kenyon, S. J., & Bromley, B. C. 2001, AJ, 121, 538

Kenyon, S. J., & Bromley, B. C. 2002, AJ, submitted

Kenyon, S. J., & Luu, J. X. 1998, AJ, 115, 2136

Kenyon, S. J., & Luu, J. X. 1999a, AJ, 118, 1101

Kenyon, S. J., & Luu, J. X. 1999b, ApJ, 526, 465

Kenyon, S. J., & Windhorst, R. 2001, ApJ, 547, L69

Kenyon, S. J., Wood, K., Whitney, B. A., & Wolff, M. 1999, ApJ, 524, L119

Kley, W. 2000, MNRAS, 313, L47

Koerner, D. W., Ressler, M. E., Werner, M. W., & Backman, D. E. 1998, ApJ, 503, L83

Kokubo, E., & Ida, S. 1996, Icarus, 123, 180

Kokubo, E., & Ida, S. 1998, Icarus, 131, 171

Kokubo, E., & Ida, S. 2000, Icarus, 143, 15

Kolvoord, R. A. & Greenberg, R. 1992, Icarus, 98, 2

Kortenkamp, S. J., & Wetherill, G. W. 2000, Icarus, 143, 60

Kowal, C. T. 1989, Icarus, 77, 118

Kuchner, M J., Brown, M. E., & Holman, M. 2002, AJ, submitted

Kuiper, G. P. 1951, in Astrophysics: A Topical Symposium, ed. J. A. Hynek (New York: McGraw-Hill), p. 357

Lada, C. J. 1999, in The Physics of Star Formation and Early Stellar Evolution, ed. C. J. Lada & N. Kylafis (Dordrecht, Kluwer), p. 143

Lagrange, A.-M., Backman, D., & Artymowicz, P. 2000, in Protostars & Planets IV, ed. V. Mannings, A. P. Boss, & S. S. Russell (Tucson: Univ. of Arizona), p. 639

Laplace, P. S. 1796, Mécanique Céleste

Larsen, J. A., et al. 2001, AJ, 121, 562

Lee, M. H. 2000, Icarus, 143, 74

Leinert, Ch. et al. 1998, A&AS, 127, 1

Levison, H. F., & Duncan, M. J. 1990, AJ, 100, 1669

Levison, H. F., & Duncan, M. J. 1993, ApJ, 406, L35

Levison, H. F., & Duncan, M. J. 1994, Icarus, 108, 18

Levison, H. F., & Duncan, M. J. 1997, Icarus, 127, 13

Levison, H. F., Lissauer, J. J., & Duncan, M. J. 1998, AJ, 116, 1998

Levison, H. F., & Stern, S. A. 1995, Lunar Planet Sci. Conf. XXVI, 841

Lin, D. N. C., & Ida, S. 1997, ApJ, 477, 781

Lin, D. N. C., & Papaloizou, J. C. B., 1995, ARA&A, 33, 505

Lin, D. N. C., & Papaloizou, J. C. B., 1996, ARA&A, 34, 703

Lissauer, J. J. 1987, Icarus, 69, 249

Lissauer, J. J. 1993, ARA&A, 31, 129

Lissauer, J. J., Pollack, J. B., Wetherill, G. W., & Stevenson, D. J. 1996, in Neptune and Triton, ed. D. P. Cruikshank, M. S. Matthews, & A. M. Schumann (Tucson: Univ. of Arizona), p. 37

Luciani, J. F., Namouni, F., & Pellat, R. 1995, ApJ, 439, 800

Lüst, R. 1952, Zs. f. Nat., 7a, 87

Luu, J. X., & Jewitt, D. 1988, AJ, 95, 1256

Luu, J. X., & Jewitt, D. 1996a, AJ, 111, 499

Luu, J. X., & Jewitt, D. 1998, ApJ, 502, L91

Luu, J. X., Jewitt, D., & Trujillo, C. A. 2000, ApJ, 531, L151

Luu, J. X., Marsden, B., Jewitt, D., Trujillo, C. A., Hergenother, C. W., Chen, J., & Offutt, W. B. 1997, Nature, 387, 573

Lynden-Bell, D., & Pringle, J. E. 1974, MNRAS, 168, 603

Malhotra, R. 1995, AJ, 110, 420

Malhotra, R. 1996, AJ, 111, 504

Malyshkin, L., & Goodman, J. 2001, Icarus, 150, 314

Mannings, V., Boss, A. P., & Russell, S. S. 2000, Protostars & Planets IV, (Tucson: Univ. of Arizona)

Morbidelli, A., & Valsecchi, G. B. 1997, Icarus, 128, 464

Nakagawa, Y., Hayashi, C., & Nakazawa, K. 1983, Icarus, 54, 361

Noll, K. S., Luu, J. X., & Gilmore, D. 2000, AJ, 119, 970

Ohtsuki, K., & Nakagawa, Y. 1988, Prog Theor Phys (Suppl), 96, 239

Ohtsuki, K., Nakagawa, Y., & Nakazawa, K. 1988, Icarus, 75, 552

Ohtsuki, K. 1999, Icarus, 137, 152

Palmer, P. L., Lin, D. N. C., & Aarseth, S. J. 1993, ApJ, 403, 336

Podolak, M., & Reynolds, R. T. 1987, Icarus, 70, 31

Podolak, M., Young, R., & Reynolds, R. 1985, Icarus, 63, 266

Pollack, J. B. 1984, ARA&A, 22, 389

Pollack, J. B., Hubickyj, O., Bodenheimer, P., Lissauer, J. J., Podolak, M., & Greenzweig, Y. 1996, Icarus, 124, 62

Rafikov, R. R. 2001, AJ, 122, 2713

Richling, S., & Yorke, H. W. 1997, A&A, 327, 317

Richling, S., & Yorke, H. W. 1998, A&A, 340, 508

Richling, S., & Yorke, H. W. 2000, ApJ, 539, 258

Russell, S. S., Srinivasan, G., Huss, G. R., Wasserburg, G. J., & Macpherson, G. J. 1996, Science, 273, 757

Safronov, V. S. 1969, Evolution of the Protoplanetary Cloud and Formation of the Earth and Planets, Nauka, Moscow [Translation 1972, NASA TT F-677]

Sasselov, D. D., & Lecar, M. 2000, ApJ, 528, 995

Schneider, G., et al. 1999, ApJ, 513, L127

Shakura, N. I., & Sunyaev, R. A. 1973, A&A, 24, 337

Shu, F. H., Johnstone, D., & Hollenbach, D. 1993, Icarus, 106, 92

Sirono, S., & Greenberg, J. M. 2000, Icarus, 145, 230

Smith, B. A., & Terrile, R. J. 1984, Science, 226, 1421

Song, I., Caillault, J.-P., Barrado y Navascués, D., & Stauffer, J. R. 2000a, ApJ, 546, 352

Spangler, C., Sargent, A. I., Silverstone, M. D., Becklin, E. E., & Zuckerman, B. 2001, ApJ, 555, 932

Spaute, D., Weidenschilling, S. J., Davis, D. R., & Marzari, F. 1991, Icarus, 92, 147

Stern, S. A. 1995, AJ, 110, 856

Stern, S. A. 1996a, AJ, 112, 1203

Stern, S. A. 1996b, A&A, 310, 999

Stern, S. A., & Colwell, J. E. 1997a, AJ, 114, 841

Stern, S. A., & Colwell, J. E. 1997b, ApJ, 490, 879

Stewart, G. R., & Ida, S. 2000, Icarus, 143, 28

Stewart, G. R., & Kaula, W. M. 1980, Icarus, 44, 154

Tanaka, H., Inaba, S., & Nakazawa, K. 1996, Icarus, 123, 450

Teplitz, V. I., Stern, S. A., Anderson, J. D., Rosenbaum, D., Scalise, R. I., & Wentzler, P. 1999, ApJ, 516, 425

Torbett, M. V., & Smoluchowski, R. 1990, Nature, 345, 49

Trujillo, C. A., & Brown, M. E. 2001, ApJ, 554, 95

Trujillo, C. A., Jewitt, D. C., & Luu, J. X. 2001a, AJ, 122, 457

Trujillo, C. A., Jewitt, D. C., Bosh, A., & Luu, J. X. 2001b, AJ, in press

Vernazza, J. E., Avrett, E. H., & Loeser, R. 1981, ApJS, 45, 635

von Weiszäcker, C. F. 1943, Zs. f. Ap., 22, 319

von Weiszäcker, C. F. 1948, Zs. f. Nat., 3a, 524

Ward, W. R. 1989, ApJ, 345, L99

Ward, W. R. 1997, Icarus, 126, 261

Ward, W. R., & Hahn, J. M. 1998, AJ, 116, 489

Weidenschilling, S. J. 1977a, Astrophys Sp Sci, 51, 153

Weidenschilling, S. J. 1977b, MNRAS, 180, 57

Weidenschilling, S. J. 1980, Icarus, 44, 172

Weidenschilling, S. J. 1984, Icarus, 60, 553

Weidenschilling, S. J., & Cuzzi, J. N., 1993, in Protostars and Planets III, ed. E. H. Levy & J. I. Lunine (Tucson: Univ of Arizona), p. 1031

Weidenschilling, S. J., & Marzari, F. 1996, Nature, 384, 619

Weidenschilling, S. J., Spaute, D., Davis, D. R., Marzari, F., & Ohtsuki, K. 1997, Icarus, 128, 429

Weissman, P. R., & Levison, H. F. 1997, in Pluto and Charon, ed. S. A. Stern, D. J. Tholen, & A. R. Schumer (Tucson: Univ of Arizona), p. 559

Wetherill, G. W. 1990a, Icarus, 88, 336

Wetherill, G. W., & Stewart, G. R. 1989, Icarus 77, 300

Wetherill, G. W., & Stewart, G. R. 1993, Icarus, 106, 190

Windhorst, R., Mathis, D. F., & Keel, W. C. 1992, ApJ, 400, L1

Windhorst, R. A., Gordon, J. M., Pascarelle, S. M., Schmidtke, P. C., Keel, W. C., Burkey, J. M., & Dunlop, J. S. 1994, ApJ, 435, 577

Windhorst, R. A., Keel, W. C., & Pascarelle, S. M. 1998, ApJ, 494, L27
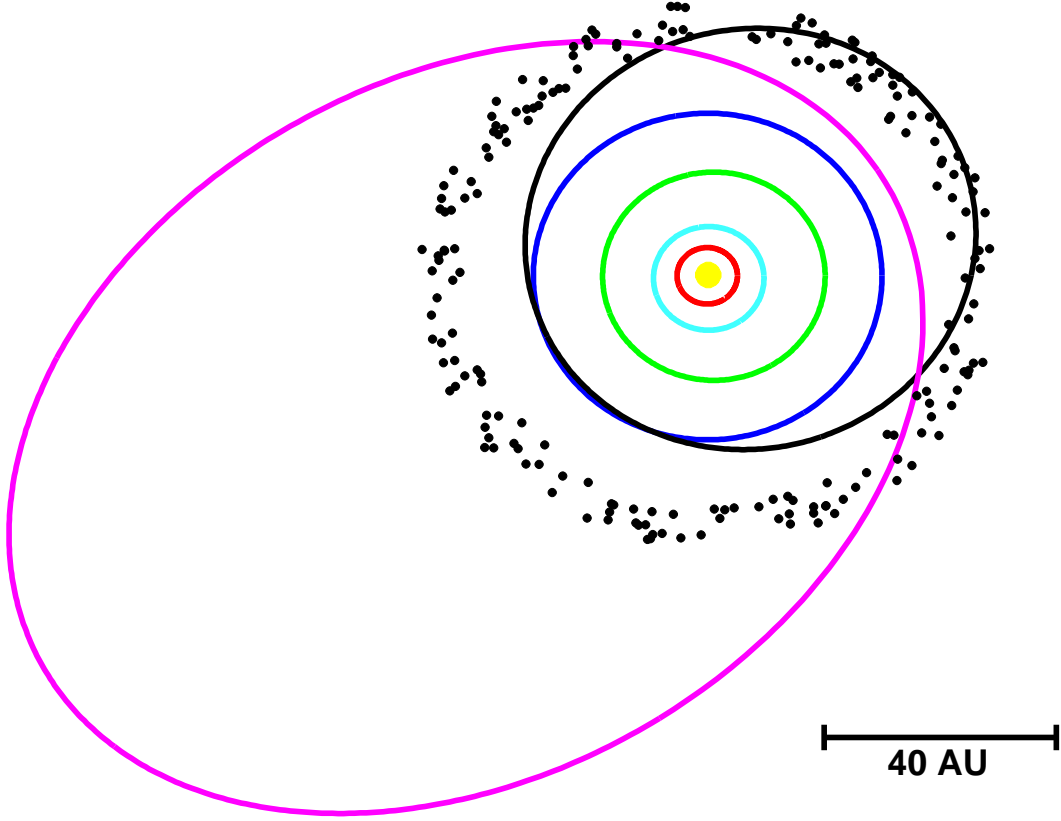
Fig. 1.— Top view of the solar system. The yellow filled circle is the Sun. Colored ellipses indicate the orbits of Jupiter (dark purple), Saturn (cyan), Uranus (green), Neptune (blue), Pluto (black), and the scattered Kuiper Belt object 1996 TL_{66} (magenta). The black dots represent 200 classical Kuiper Belt objects randomly distributed in a band between 42 AU and 50 AU. The bar at the lower right indicates a distance of 40 AU.
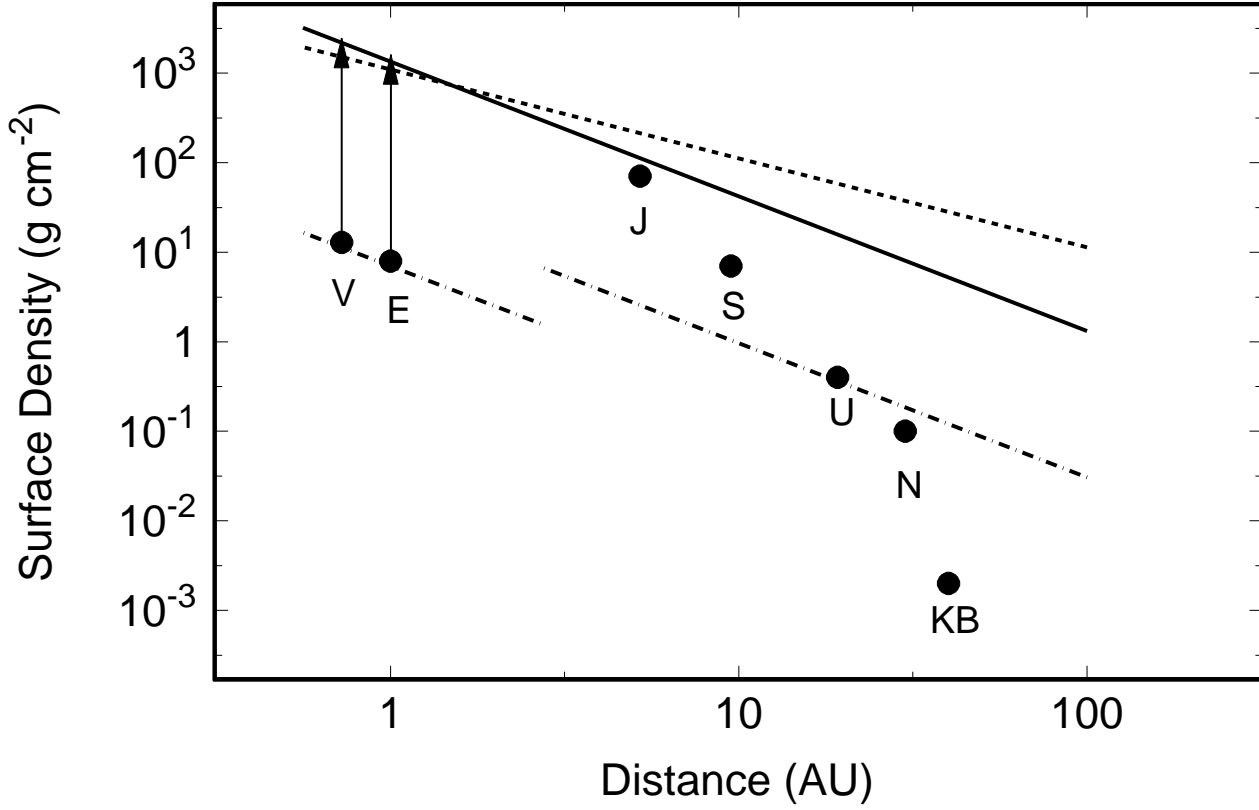
Fig. 2.— Surface density distribution in the solar system, assuming that the mass is spread uniformly over an annulus centered on the orbit of the planet. The arrows indicate the surface density for terrestrial planets if augmented to a solar abundance of hydrogen and helium. The solid and dot-dashed curves indicate $\Sigma \propto A^{-3/2}$ (Weidenschilling 1977a; Hayashi 1981); the dashed line indicates $\Sigma \propto A^{-1}$ (Cameron 1995).
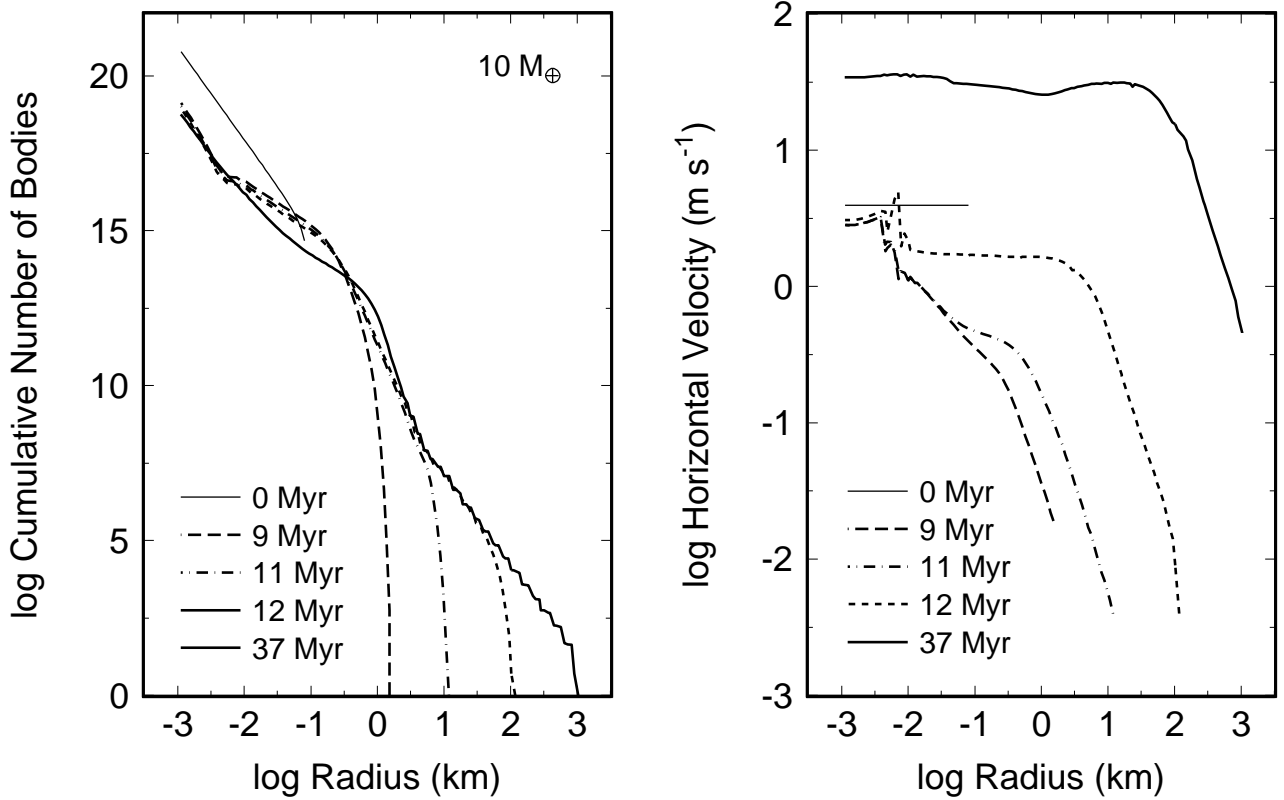
Fig. 3.— Evolution of a single annulus coagulation model with $M_0 = 10\ M_{\oplus}$, $e_0 = 10^{-3}$, and $S_0 = 2 \times 10^6$ erg g^{-1}: (a) cumulative size distribution (left panel), and (b) horizontal velocity (right panel) as a function of time. Collisional growth is quasi-linear until the largest bodies have r_{max} = 1–2 km at 9–10 Myr. Collisional damping reduces the velocities of all bodies to $\sim$ 1–2 m s^{-1} on this timescale; dynamical friction damps the velocities of larger bodies to $\sim 10^{-2}$ m s^{-1}. Runaway growth then produces objects with radii of 100 km in another 2–3 Myr. Viscous stirring heats up particle velocities as objects grow to sizes of 100–300 km. Runaway growth ends. A prolonged oligarchic growth phase leads to the production of 1000 km objects; the horizontal velocities are then $\sim$ 30–40 m s^{-1} for the smallest objects and $\sim$ 1 m s^{-1} for the largest objects. Adapted from Kenyon & Luu (1999a)
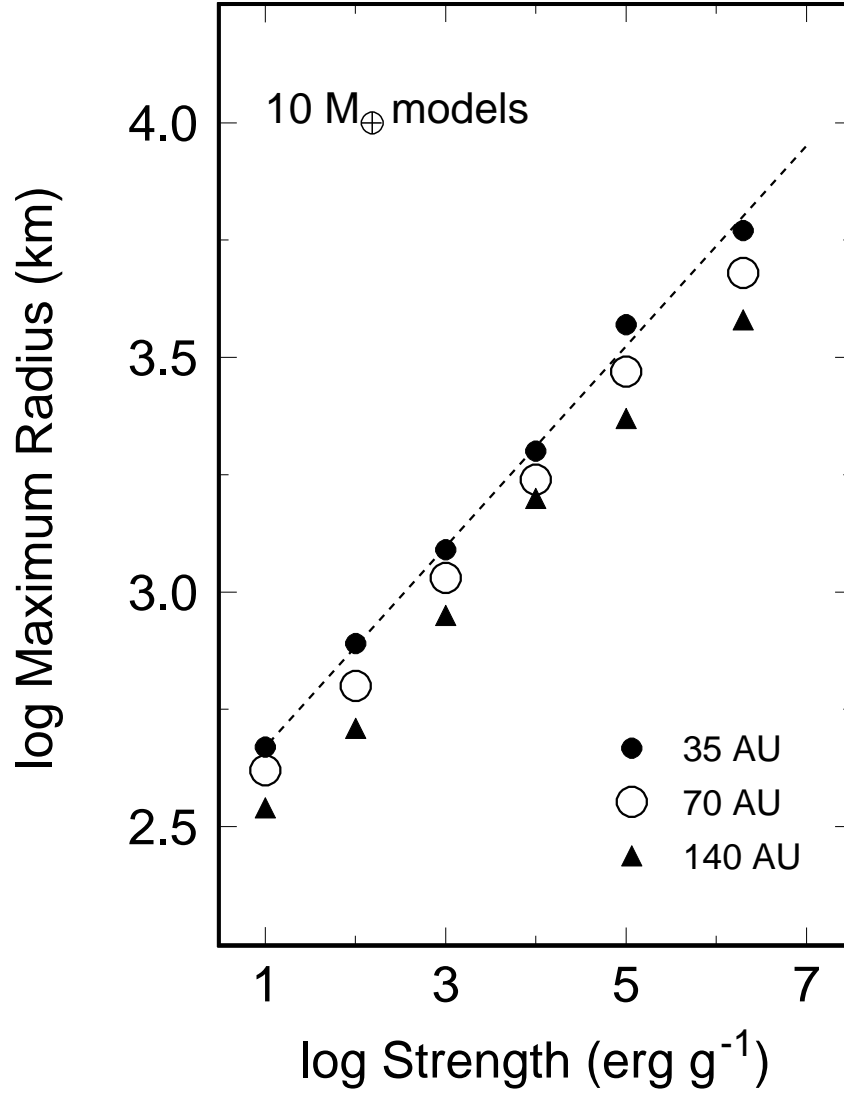
Fig. 4.— Maximum radius as a function of tensile strength and heliocentric distance for single annulus models with $M_0 = 10$ $M_\oplus$ and $e_0 = 10^{-4}$. At a given heliocentric distance, larger planets grow from stronger planetesimals. At a given tensile strength, smaller planets form at larger heliocentric distances. Adapted from Kenyon & Luu (1999a).
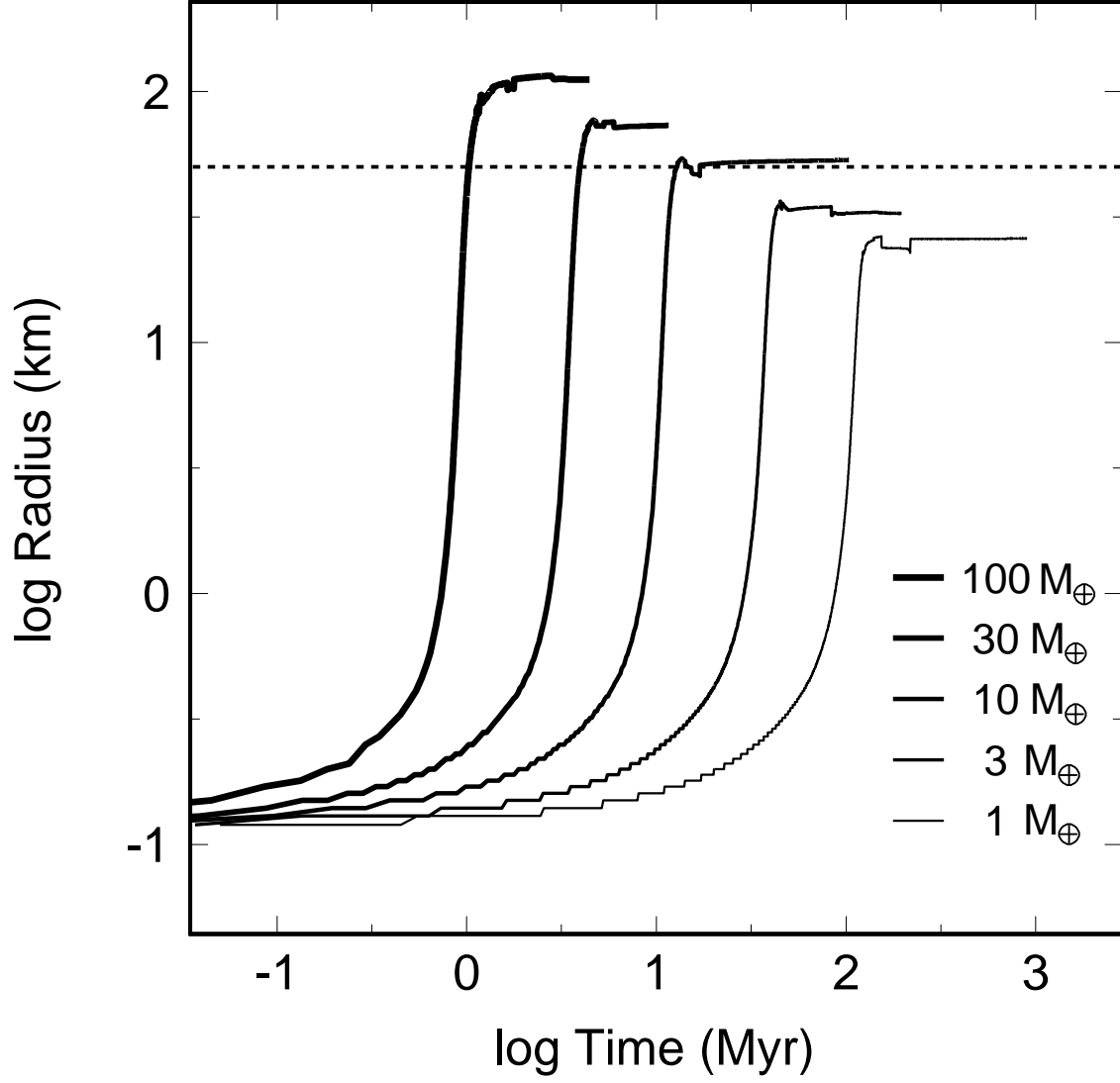
Fig. 5.— Evolution of r_5, the radius where the cumulative number of objects is 10^5, with time as a function of initial mass, M_0, for single annulus models with $e_0 = 10^{-3}$. The horizontal dashed line indicates the constraint on r_5 set by current observations. Adapted from Kenyon & Luu (1999a).
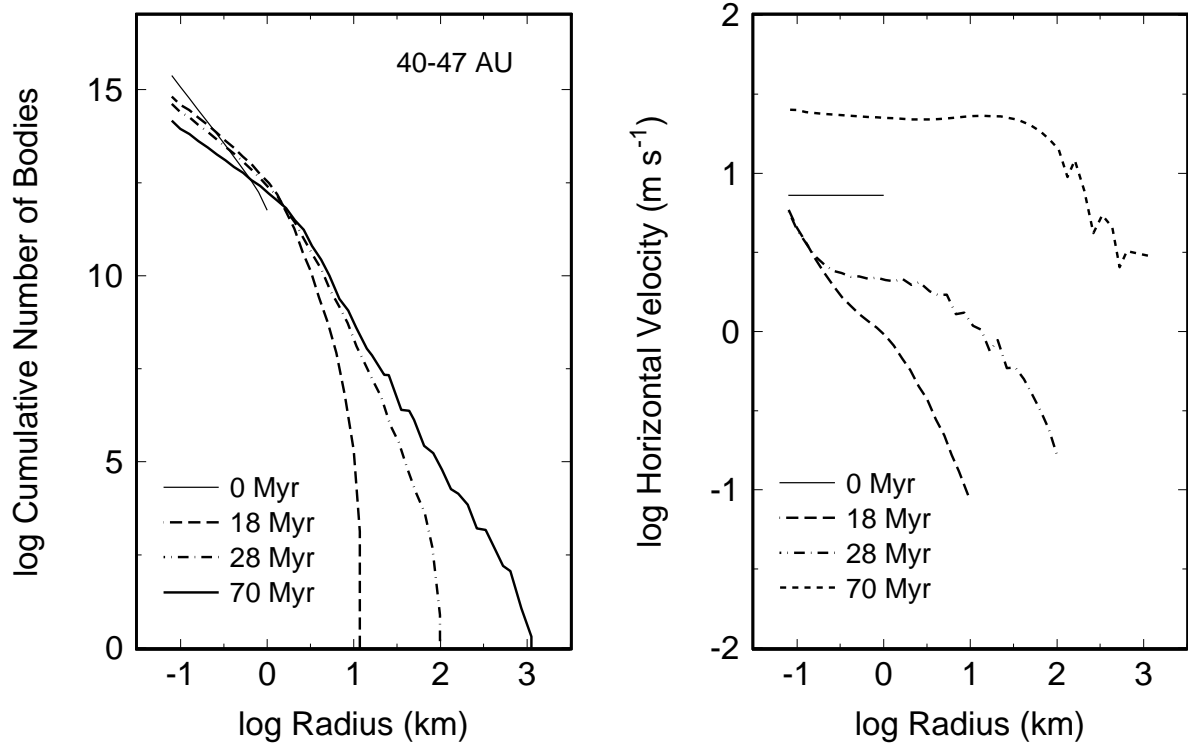
Fig. 6.— Evolution of a multiannulus coagulation model with $\Sigma_i = 0.3 \ (a_i/35 \ \mathrm{AU})^{-3/2}$, $e_0 = 2 \times 10^{-3}$, $S_0 = 2 \times 10^6 \ \mathrm{erg \ g^{-1}}$, and velocity evolution: (a) cumulative size distribution (left panel), and (b) horizontal velocity (right panel)as a function of time. Collisional growth is quasi-linear until the largest bodies have $r_{max} = 3$–10 km at 20 Myr. Collisional damping reduces the velocities of small bodies to ~ 1–5 m s^{-1} on this timescale; dynamical friction reduces the velocities of larger bodes to $\lesssim 10^{-1}$ m s^{-1}. Runaway growth then produces objects with radii of 100 km in 10 Myr. Viscous stirring increases particle velocities as objects grow to sizes of 300–500 km, and runaway growth ends. An oligarchic growth phase leads to the production of 1000 km objects after ~ 70 Myr; the horizontal velocities are then ~ 40–50 m s^{-1} for the smallest objects and ~ 2–3 m s^{-1} for the largest objects.
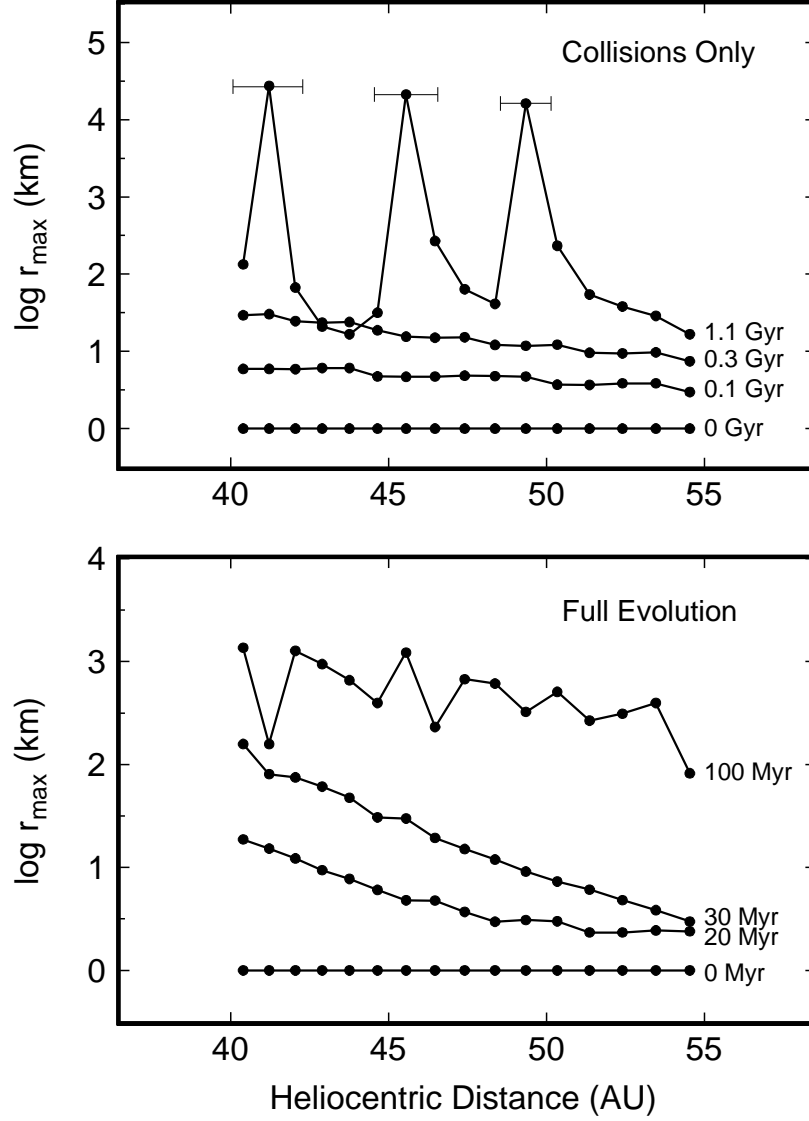
Fig. 7.— Mass of the largest body in each annulus of two multiannulus coagulation calculations. (a) top panel: the radius of the largest object at 0, 0.1, 0.3, and 1.1 Gyr for a model without velocity evolution; (b) bottom panel: the radius of the largest object at 0, 20, 30, and 100 Myr for a model with velocity evolution. Each annulus initially contains 0.1–1 km bodies with the surface density in solid material equivalent to a Minimum Mass Solar Nebula. Objects grow faster in models with velocity evolution, but objects become larger in models without velocity evolution. The error bars in the top panel indicate the Hills radius R_H for each large body formed in the calculation without velocity evolution. Objects cannot accrete material beyond 2.4 R_H (see also Alexander & Agnor 1998; Kokubo & Ida 1998).
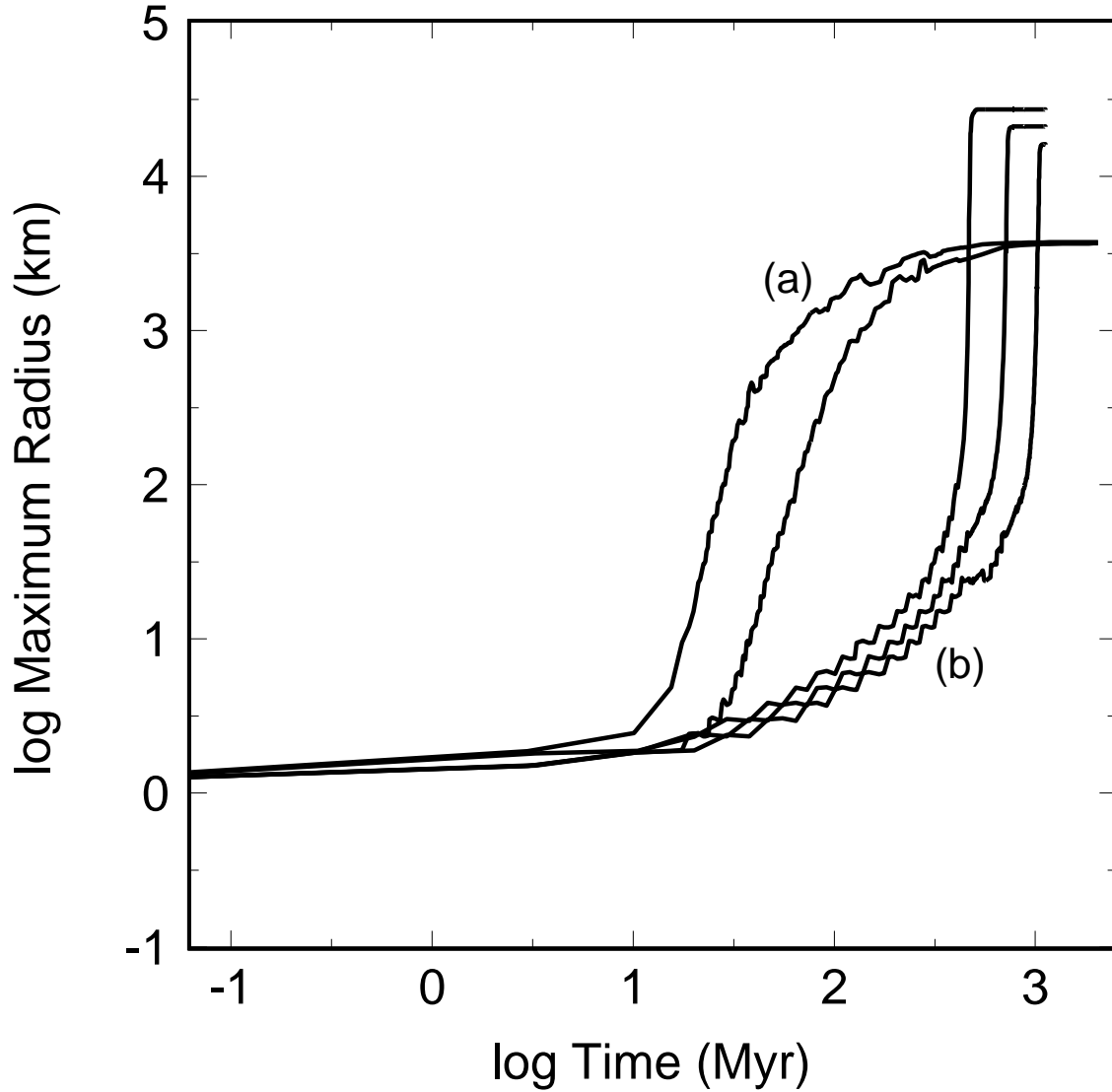
Fig. 8.— Evolution of the largest objects in several multiannulus calculations of planetesimal evolution at 40–55 AU. The two curves labeled '(a)' show the growth of the largest objects in a multiannulus calculation with velocity evolution and fragmentation (Figure 6). The first curve plots the growth of the largest object in annulus (1); the second curve plots the growth of the largest object in annulus (15). The curves labeled '(b)' show the growth of the largest objects in a calculation with fragmentation but no velocity evolution (Figure 7). The largest object in annulus (2) reaches runaway growth before the largest object in annulus (7), which achieves its maximum radius before the largest object in annulus (11) begins runaway growth.
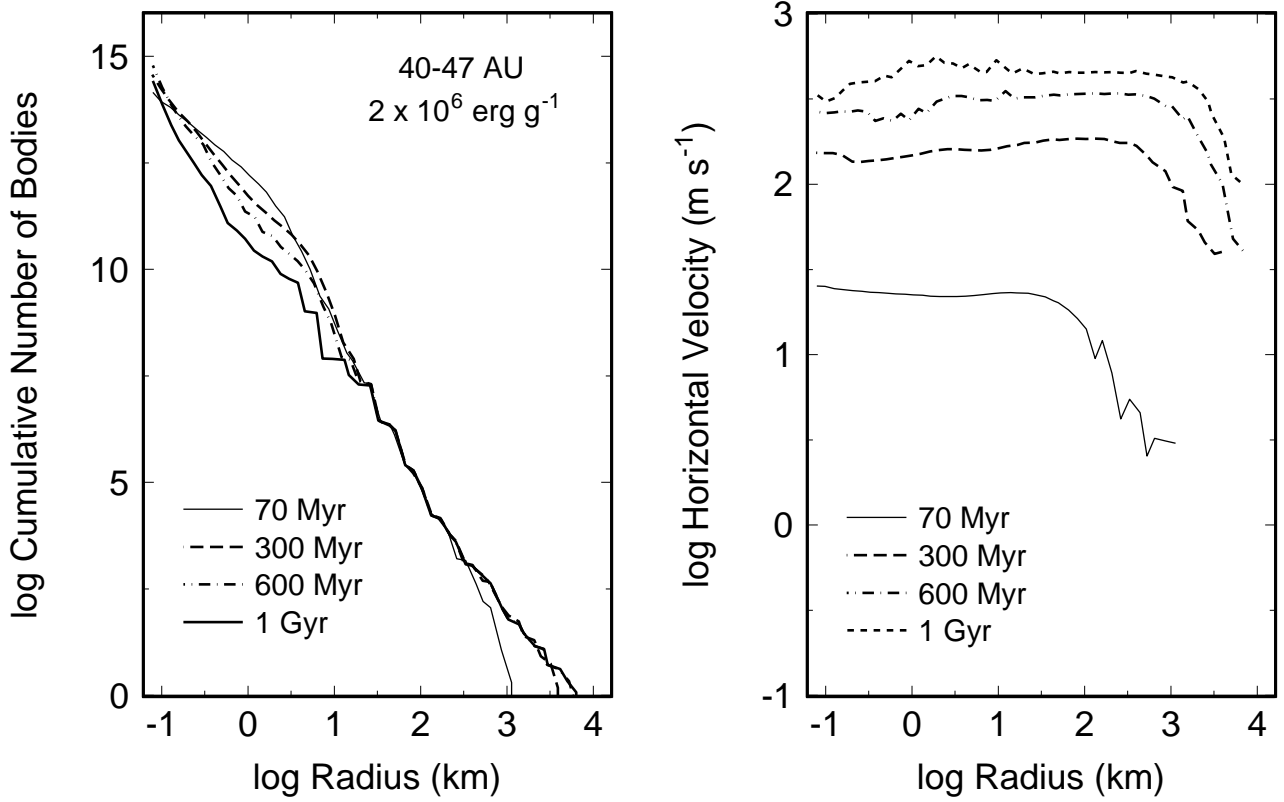
Fig. 9.— Late evolution of a multiannulus model with $\Sigma_i = 0.3 \ (a_i/35 \ \mathrm{AU})^{-3/2}$, $e_0 = 2 \times 10^{-3}$, $S_0 = 2 \times 10^6$ erg g^{-1}, and velocity evolution: (a) cumulative size distribution (left panel), and (b) horizontal velocity (right panel) as a function of time. After the first Pluto-sized object forms at $\sim$ 70 Myr, growth is oligarchic. As objects grow from radii of $\sim$ 1000 km to radii of $\sim$ 6000 km, viscous stirring increases particle velocities to the shattering limit. Shattering reduces the population of 1–10 km objects on timescales of 500 Myr to 1 Gyr.
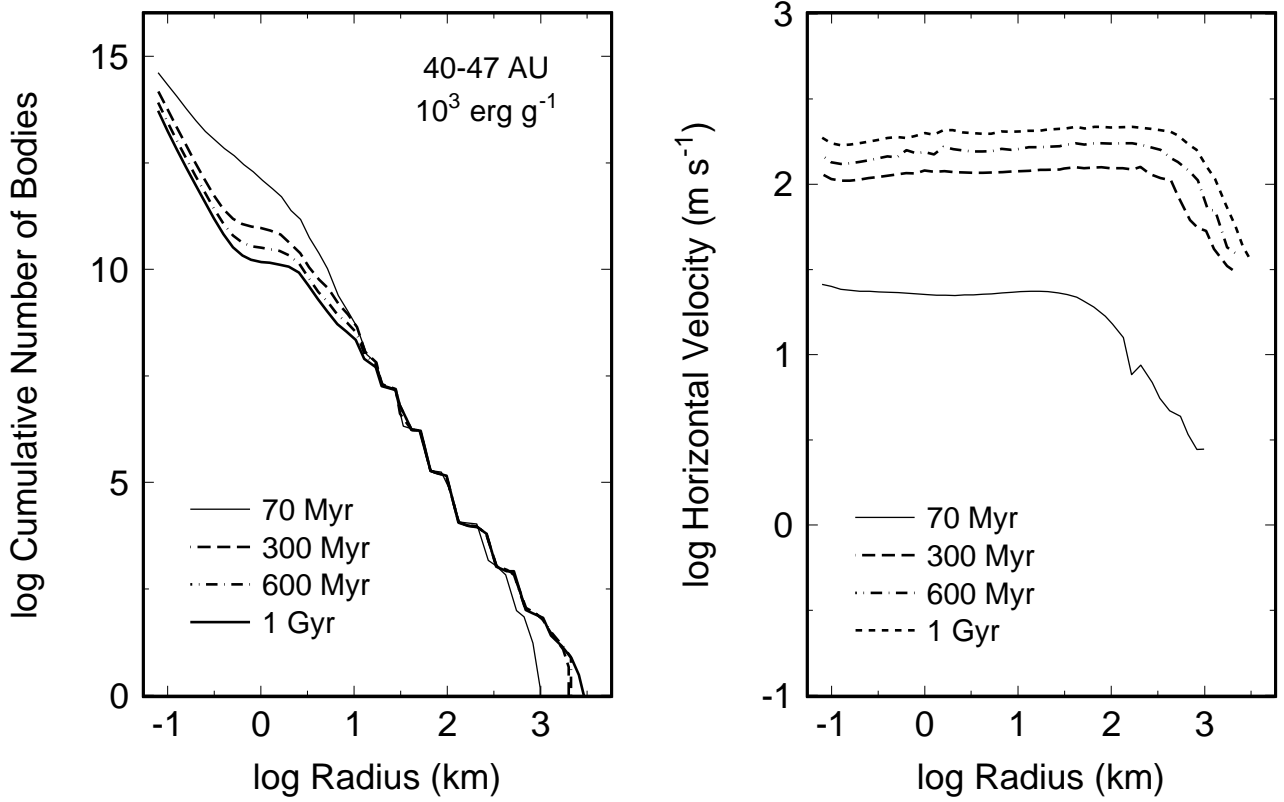
Fig. 10.— Late evolution of a multiannulus model with $\Sigma_i = 0.3\ (a_i/35\ \mathrm{AU})^{-3/2}$, $e_0 = 2 \times 10^{-3}$, $S_0 = 10^3$ erg g^{-1}, and velocity evolution: (a) cumulative size distribution (left panel), and (b) horizontal velocity (right panel) as a function of time. After the first Pluto-sized object forms at ~ 70 Myr, growth is oligarchic. As objects grow from radii of ~ 1000 km to radii of ~ 3000 km, viscous stirring increases particle velocities to the shattering limit. At times of 300 Myr to 1 Gyr, shattering reduces the population of small objects and produces a prominent dip in the size distribution at 0.3–3 km.
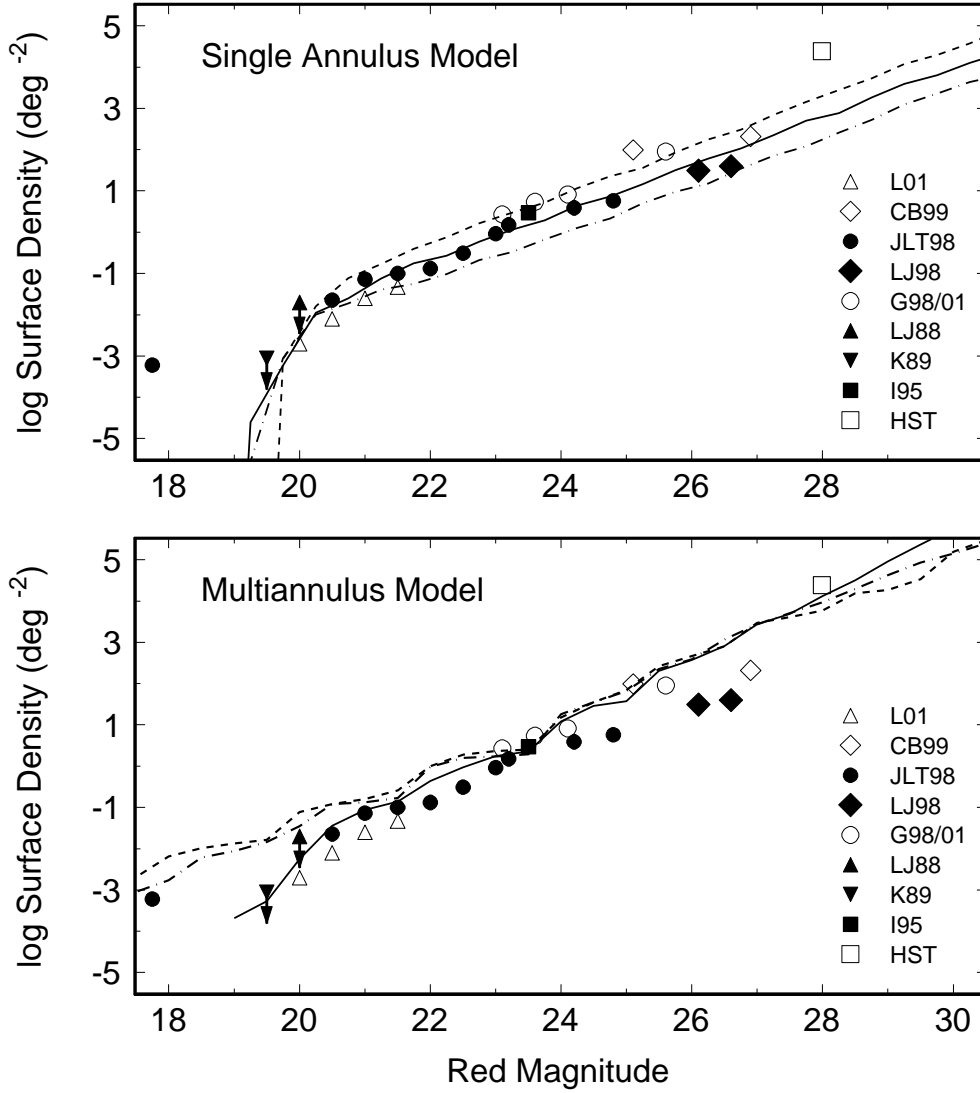
Fig. 11.— Comparison of model luminosity functions of KBOs with observations. Data are as indicated in the legend of each panel and are from Cochran et al. (1998; HST), Irwin et al. (1995; I95), Kowal 1989 (1989; K89), Luu & Jewitt (1988; LJ88), Gladman et al. (1998, 2001; G98/01), Luu & Jewitt (1998; LJ98), Jewitt et al. (1998; JLT98), Chiang & Brown (1999; CB99), and Larsen et al. (2001; L01). Error bars for each datum – typically a factor of 2–3 – and the upper limit from Levison & Duncan (1990) are not shown for clarity. The lines plot luminosity functions for (a) upper panel: single annulus models at 35 AU with $e_0 = 10^{-3}$ and $M_0 \approx 0.3$ (dot-dashed), 1.0 (solid), and 3.0 (dashed) times the Minimum Mass Solar Nebula and (b) lower panel: multiannulus models at 40–55 AU for models with a mass in solids of a Minimum Mass Solar Nebula with $e_0 = 2 \times 10^{-3}$ and $S_0 = 2 \times 10^6$ erg g^{-1} (solid line: 70 Myr; dashed line: 1 Gyr) and $S_0 = 10^3$ erg g^{-1} (dot-dashed line: 1 Gyr).
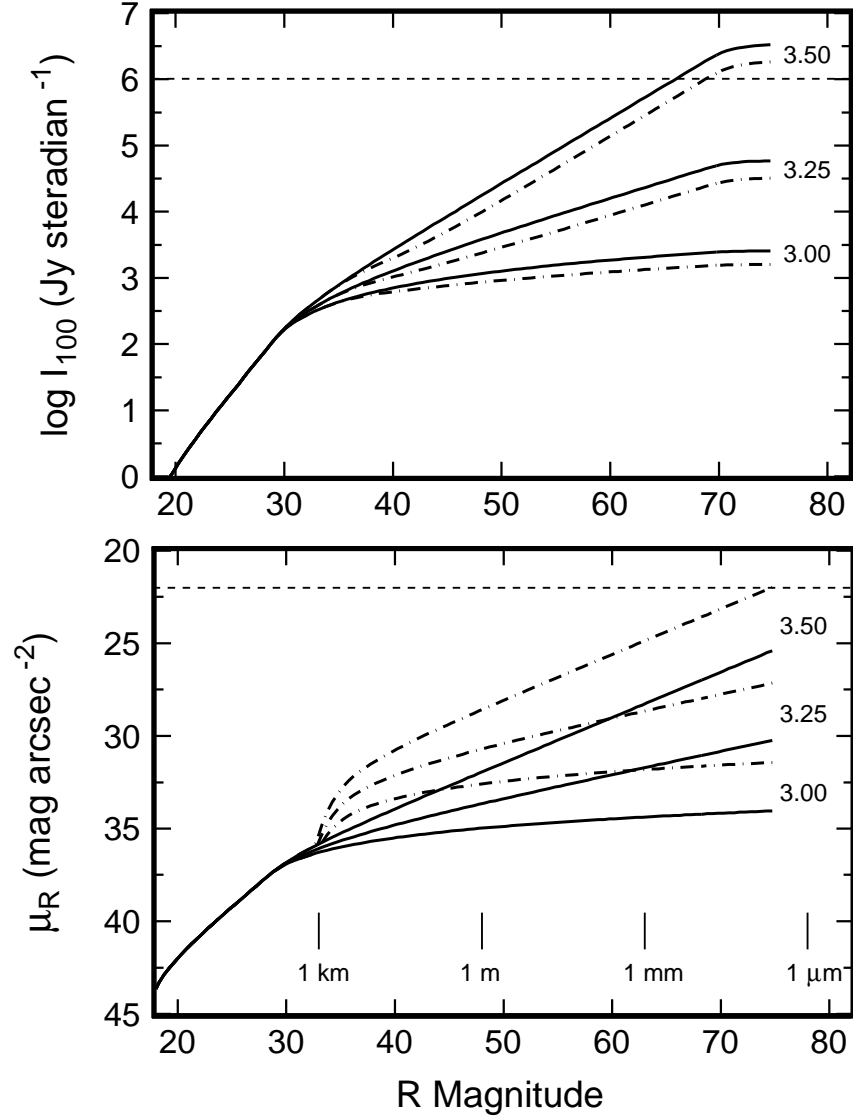
Fig. 12.— Far-infrared and optical surface brightness as a function of R magnitude for a physical model of KBO grains. The model assumes a broken power law size distribution, equation (11), albedo ω_g, and a surface density distribution for KBOs in a ring at 40–50 AU. Solid curves show results for $a_1 = 3$, $\omega = 0.04$, and a_2 as indicated at the right end of each curve. Dot-dashed curves repeat this model for small grains with larger ω. Each model is consistent with observations of the optical counts at $R \leq 26$–27.